

The Millennium Run Observatory: First Light

R. Overzier^{1,†*}, G. Lemson², R.E. Angulo^{3,2}, E. Bertin⁴, J. Blaizot⁵, B.M.B. Henriques²,
G.-D. Marleau^{6,7}, S.D.M. White²

¹*Department of Astronomy, The University of Texas at Austin, 2515 Speedway, Stop C1400, Austin, TX 78712-1205, USA*

²*Max-Planck-Institut für Astrophysik, D-85748 Garching, Germany*

³*Kavli Institute for Particle Astrophysics and Cosmology, Stanford University, 452 Lomita Mall, Stanford, CA 94305-4085, USA*

⁴*Institut d'Astrophysique de Paris, 98 bis Boulevard Arago, 75014, Paris, France*

⁵*Université de Lyon, Lyon F-69003, France; Université Lyon 1, Observatoire de Lyon, 9 Avenue Charles André, Saint-Genis Laval F-69230, France;*

CNRS, UMR 5574, Centre de Recherche Astrophysique de Lyon, France; Ecole Normale Supérieure de Lyon, Lyon F-69007, France

⁶*Max-Planck Institut für Astronomie, Königstuhl 17, D-69117 Heidelberg, Germany*

⁷*Department of Physics, McGill University, 3600 Rue University, Montréal, QC H3A 2T8, Canada*

[†] *UT Prize Fellow*

ABSTRACT

Simulations of galaxy evolution aim to capture our current understanding as well as to make predictions for testing by future experiments. Simulations and observations are often compared in an indirect fashion: physical quantities are estimated from the observational data and compared to models. However, many applications can benefit from a more direct approach, where the observing process is also simulated, so that the models are seen fully from the observer's perspective. To facilitate this, we have developed the Millennium Run Observatory (MRObs), a theoretical virtual observatory which uses virtual telescopes to 'observe' semi-analytic galaxy formation simulations based on the suite of Millennium Run (MR) dark matter simulations. The MRObs produces data that can be processed and analyzed using the standard observational software packages developed for real observations. At present, we produce images in forty filters covering the rest-frame UV to infrared for two stellar population synthesis models, for three different models of absorption by the intergalactic medium, and in two cosmologies (WMAP1 and 7). Galaxy distributions for a large number of mock lightcones can be 'observed' using models of major ground- and space-based telescopes. The data include lightcone catalogues linked to structural properties of galaxies, pre-observation model images, mock telescope images, and Source Extractor products that can all be traced back to the higher-level dark matter, semi-analytic galaxy, and lightcone catalogues available in the MR database. Here, we describe our methods and announce a first public release of simulated observations that emulate a large number of extra-galactic surveys (e.g. SDSS, CFHT-LS, GOODS, GOODS/ERS, CANDELS, and HUDF). The MRObs browser, an online tool, further facilitates exploration of the simulated data. We demonstrate the benefits of a direct approach through a number of example applications: (1) deep galaxy number counts in the CANDELS survey; (2) observed properties of galaxy clusters; (3) structural parameters of galaxies; and (4) identification of drop-out galaxies. The MRObs enhances the range of questions that can be asked of semi-analytic models, allowing observers and theorists to work toward each other with virtually complete freedom of where to meet.

Key words: Astronomical Data bases – cosmology: theory – cosmology: observations – large-scale structure of Universe – galaxies: evolution – galaxies: clusters: general

1 INTRODUCTION

Understanding formation and evolution of galaxies is one of the main goals of extra-galactic astrophysics. This study is approached from two sides, an observational one and a theoretical one. On the

one hand, observations become more and more detailed, producing ever larger images and catalogues that need to be analyzed. On the other hand, theoretical research produces ever more refined models describing the formation and evolutionary processes in ever greater detail, often using sophisticated cosmological computer simulations that create enormous, physically motivated data sets. The increasing specialization and technical sophistication required means that it becomes a problem to successfully match these

* E-mail: overzier@astro.as.utexas.edu (RO)

two approaches as few scientists are familiar with all the details on both the observational and the theoretical side. For example, it is often difficult for non-experts to understand detailed galaxy formation models or to predict how model parameter changes affect the predictions. Likewise, theorists are often unfamiliar with the extensive processing and the inverse methods that need to be applied to observations in order to derive physical properties that can be matched to the model predictions.

From an observational perspective, the Sloan Digital Sky Survey (SDSS) consortium played a pivotal role in opening up the results of one of the most sophisticated observational programs ever performed to the community. Through a public database of raw measurements, processed results, and ‘value-added’ products, a great many hurdles were removed for using the results of the survey. From a theoretical perspective, the Millennium Run Database (MRDB) was the first to make the results of large scale cosmological simulations widely accessible to a broad-based audience. Analogous to the SDSS data, the richness of the theoretical data sets available in the MRDB has allowed a wide variety of scientific queries to be performed.

The comparison between cosmological model predictions and observations has historically been performed mostly in one direction only: physical quantities estimated from observations are compared with theoretical predictions. The latter are not affected by the issues that affect the observations, such as incompleteness, contamination, cosmic variance, finite signal-to-noise, or limited resolution. These are typically assumed to be corrected for in full during the processing of the observations, although some authors have included some of these effects in a number of ways in order to be able to more realistically compare data and predictions (e.g. Baugh et al. 1998; Blaizot et al. 2004; Marinoni et al. 2005; Pollo et al. 2006; Guo & White 2009; Overzier et al. 2009a; de la Torre et al. 2011; Cucciati et al. 2012; Pforr et al. 2012).

We propose that the comparison between models and observations should also be performed in the opposite direction. The strength of this method lies in the fact that one can never be sure to extract the truth out of observations, but one will always know what the true answer is in a set of synthetic observations based on the simulations. Synthetic observations like we propose would also allow one to explore the uniqueness of possible solutions that are found, as different models or different parameter sets may produce indistinguishable synthetic observations. In this paper we present an extension of the MR cosmological simulations project, which we will henceforth refer to as the *Millennium Run Observatory* (MRObs). It aims to bridge the gap between the two approaches by making the final step from realistic simulations to the observational plane. MRObs consists of a fully connected set of synthetic data products combined into a unique online framework that ranges from the most fundamental simulations to realistic, synthetic observations.

With the introduction of ‘lightcones’, the comparison between simulations and observations has been greatly enhanced. This technique allows one to project the galaxy distribution predicted for a set of discrete simulation snapshots along a virtual observer’s line of sight, mimicking the main geometric and photometric effects present in deep galaxy surveys (Davis et al. 1982, 1985; Cole et al. 1998; Diaferio et al. 1999; Blaizot et al. 2005; Kitzbichler & White 2007). However, even the lightcone approach to model-data comparisons is still very much idealized. To illustrate this, let us consider a typical observational scenario of determining the stellar mass function of high redshift galaxies in a multi-wavelength imaging survey. Such an analysis typically begins with the extraction of

sources and their photometric properties across a set of calibrated and registered filter images. Due to missed light, it is often necessary to make corrections to the measured magnitudes. Then, photometric redshifts and physical parameters of the galaxies (e.g., stellar mass, age, SFR) are estimated by fitting the photometry with a set of template galaxy spectra. It is important to note that the results often depend on, e.g., the source detection and photometry method, the choice of template spectra, and the fitting method. In order to calculate the number of galaxies detected in different stellar mass bins over different redshift intervals, it is often required to calculate the ‘effective volume’ of the survey. The latter is an estimate of the completeness of the sample, and usually depends on redshift, limiting magnitude, galaxy colour or size in complicated ways. This last step can be performed by estimating the probability of recovering certain sources at a given survey depth. Such estimates typically depend on the true source population which is a priori unknown. At the end of the process, the stellar mass function estimate is used for comparison with other observational studies, or to constrain certain theoretical models or simulations of galaxy formation. It should be clear from the process outlined above that a great number of non-trivial steps need to be performed before any comparison with theory can be made. How better could we test all these steps than by processing the output from the simulations, for which all quantities are exactly known, through the same kind of data analysis pipeline as the real observations?

1.1 Goals of the MRObs

We will take the process of simulating the galaxy population for comparison with observations into largely unexplored territory by simulating the observational process applied to the MR simulations. The main aims of the MRObs are as follows:

- Extend the MR project approach by producing data products most directly corresponding to observations, namely synthetic images and extracted source catalogs
- Aid theorists in testing analytical models to observations
- Aid observers in making detailed predictions for observations and better analyses of observational data
- Allow the community to subject the models to new kinds of tests
- Allow observers and theorists to work toward each other from either direction with the freedom of where to meet
- Allow detailed comparisons with synthetic observations produced by other groups performing cosmological simulations
- Allow calibration of observational analysis methods by making available synthetic data for which the entire underlying ‘reality’ is known
- Extend the realism with which semi-analytic models can address questions such as what is the probability that a $z \sim 10$ galaxy will be detected within a particular observational data set?
- Provide a framework for future virtual theoretical observatories

1.2 Connection to previous work

Only recently have simulations become sophisticated enough to allow realistic visualizations of the galaxy population on a cosmological scale. In order to illustrate the particular place that the MRObs occupies within this simulations landscape, we give a short overview of related work in the literature. Astronomical image simulation software has been developed and used previously, mostly to aid in the development of data processing pipelines for new telescopes and instruments, for proposal planning, or for testing the accuracy of specific measurement tools (e.g. Bertin 2009; Dobke et al. 2010). Within the gravitational lensing community, it has been standard practice to use simulated data to assess the accuracy of cosmic shear measurements (Erben et al. 2001; Heymans et al. 2006; Forero-Romero et al. 2007). Simple galaxy evolution models have been coupled to image simulators to compare with observations (e.g. Bouwens et al. 1999, 2006), and mock telescope data based on semi-analytic models (SAMs) are also currently being used to investigate the significant data and science challenges posed by future surveys (e.g., with the Large Synoptic Survey Telescope (LSST); Connolly et al. 2010; Gibson et al. 2011). The detailed morphological and kinematical structures of gas and stars have been modeled using high-resolution, hydrodynamical simulations (of dark matter, gas and stars), coupled with radiative transfer models that allow one to study the effects of dust and orientation as a function of wavelength (e.g. Jonsson et al. 2006, 2010; Robertson & Bullock 2008; Wuyts et al. 2009; Chilingarian et al. 2010; Lotz et al. 2008, 2010). However, hydrodynamical simulations of sufficient resolution are currently too small to construct lightcones on cosmological scales. Also, unlike SAMs, it is a much more time-consuming process to match N -body hydro simulations to observations after each change in the sub-grid physics modeling. As a result current hydro simulations of the galaxy population are substantially further from the observations than semi-analytical models.

Blaizot et al. (2005) pioneered in the production of realistic artificial telescope data based on lightcones extracted from their semi-analytic model. That paper already laid out most of the workflow that we use here (see Fig. 1): dark matter particle simulations are used to construct halo merger trees on which a semi-analytic model is run. The output from the SAM is used to construct galaxy lightcones that are used as input for artificial telescope image simulations. Galaxies are extracted from the artificial images using standard observational tools (e.g. SExtractor; Bertin & Arnouts 1996), and the resulting galaxy catalogs are compared to the original simulations at different levels, or to actual observations. Unfortunately, however, the methods of Blaizot et al. (2005) were never employed on a large scale, and in subsequent years the comparison between SAMs and real observations has been mostly performed at the lightcone level or even at the snapshot level, thereby sidestepping many of the details involved in analyzing real telescope data that observers typically have to go through. As we shall show, however, numerous problems in the field of galaxy evolution could benefit from a simulation that accounts for the entire observational process. This leads to new insights involving details that are missed by higher-level comparisons between data and simulations. By expanding on the basic ideas of Blaizot et al. (2005), the MRObs aims at making this possible.

1.3 Why the Millennium Simulations?

Although in this paper we lay out the motivation and framework for producing synthetic data from cosmological simulations in general, the MRObs is based around the suite of MR simulations. Through the combination of simulations volume and particle resolution, an active development of semi-analytic models, and an online database providing access to numerous data products, the MR is ideally suited for most of our purposes, as follows.

(1) Volume and resolution: The MR has an almost ideal combination of volume and particle mass resolution suitable for a wide range of applications. The resolution¹ is sufficient to identify the $\gtrsim 5 \times 10^{10} M_{\odot}$ halos believed to host faint galaxies at very high redshifts (Ouchi et al. 2005; Overzier et al. 2006), while probing significantly down the stellar mass function with good statistics at lower redshifts. The volume is large enough to probe a very wide range of environments. The MR contains about 3,000 cluster-sized objects at $z = 0$, of which about 25 are of the Coma-type (i.e., more massive than $10^{15} M_{\odot}$). The formation of all these systems can be traced back to very high redshift for detailed studies of cluster formation (Overzier et al. 2009a). The large volume is also crucial for constructing synthetic galaxy surveys covering many square degrees without significant replications (Kitzbichler & White 2007; Guo & White 2009; Overzier et al. 2009a; Henriques et al. 2012).

More recent dark matter simulations have been performed. The MultiDark simulations span an $8\times$ larger volume but with a $10\times$ lower mass resolution compared to the MR (Prada et al. 2012). The Bolshoi simulations have a $10\times$ higher mass resolution, but are $8\times$ smaller (Klypin et al. 2011). Neither simulation has yet released semi-analytic galaxy catalogs that can be used to compare with actual observations. The somewhat limited mass resolution of the MR has recently been extended by two orders of magnitude through the MR-II simulation (Boylan-Kolchin et al. 2009). This simulation is extremely useful for further improving the semi-analytic model that can then be re-applied to the original MR simulation (Guo et al. 2011). The somewhat limited volume of the MR has also recently been extended by two orders of magnitude through the Millennium XXL (MXXL) simulation (Angulo et al. 2012), useful for studies of the rarest, most massive objects. However, for the generation of mock lightcones, the MR is currently still our preferred simulation ($125\times$ larger volume compared to the MR-II and $7\times$ higher resolution compared to the MXXL).

Recently, it has become possible to re-cast the suite of MR simulation results in more updated cosmologies relative to WMAP1 thanks to the re-scaling technique of Angulo & White (2010, see §2.1.1).

(2) Semi-analytic models: As we will show, the Guo et al. (2011) semi-analytic model applied to the MR is key to producing our synthetic observations. This model gives detailed predictions for the evolving sizes and spin axes of the stellar mass in disks and/or bulges that are crucial for calculating angular sizes, bulge-to-disk ratios, inclinations and position angles.

(3) MR database: The dark matter and galaxy catalogs of the MR project and related simulations have been made widely accessible to the community through the MRDB (Lemson & Virgo Consortium 2006). Interested users can query the data in this database through various online services using standard Structured Query Language (SQL). Regular updates to the MRDB holdings provide public access to the latest model results,

¹ Full convergence between the MR and the much higher resolution MR-II simulation is near $10^{11} M_{\odot}$.

ensuring that anyone can analyze the MR data and use its results in their publications. We have now added to this system our synthetic imaging data and extracted source catalogs that can be cross-correlated with the underlying simulations data in the MRDB.

In summary, despite the age of the original MR (Springel et al. 2005), more recent dark matter simulations do not yet provide equivalent data sets or the infrastructure required for developing a facility such as the MRObs.

1.4 This paper

In this paper, the first in a series comparing theory and observations in the observational plane, we lay a framework for producing synthetic data from cosmological simulations, describe our main methods for future reference, present a number of user examples, and announce the public release of a large number of simulated surveys (synthetic images and catalogs). We also present various new online services that allow one to interact with the synthetic observations and the underlying lightcones, semi-analytic galaxy and dark matter catalogs in the MRDB. The structure of this paper is as follows. In §2 we will present a concise overview of the MRObs and describe in detail all the steps that are needed in order to go from a pure dark matter simulation and semi-analytic galaxy catalog to producing realistic synthetic observations. In §3 we present a detailed simulations example focusing on our synthetic images produced for the on-going CANDELS HST program. In §4 we illustrate the new types of questions that can be asked of the MRObs through a number of examples related to galaxy and galaxy cluster evolution. In §5 we present the public data release and the interactive online tools we have developed. In §6 and §7, respectively, we present a brief outlook to future developments related to the MRObs project and summarize our results.

2 STRUCTURE OF THE MILLENNIUM RUN OBSERVATORY

The MRObs makes available a fully interconnected set of data products covering the entire chain from dark matter simulations to synthetic observations and extracted data. In the MRObs, each subsequent step uses data products produced by previous steps, and almost all the data products are available for interrogation and public download for further analysis. A schematic overview of this process is given in the workflow diagram in Fig. 1, where rectangles indicate an action and tilted rectangles represent data products that in each step can be linked to products elsewhere along the chain. The main steps are:

1. Dark matter particle simulation (DM density fields)
2. Identifying of friends-of-friends (FOF) groups
3. Identifying (sub-)halos
4. Constructing halo merger trees
5. Applying semi-analytic galaxy models
6. Observing galaxies on a synthetic light-cone
7. Producing synthetic telescope images

8. Extracting sources from synthetic images

In this section we will describe each of the steps in more detail, focusing on the newly developed components that are most essential to bridge the gap to real observations (steps 6–8), and refer to other work for the components described in detail elsewhere (steps 1–5).

2.1 The Millennium suite of dark matter simulations

The evolution of the dark matter distribution with time is believed to be mainly driven by the initial matter power spectrum, gravity, and the expansion rate of the universe, and can be taken either from direct N -body simulations (e.g. Davis et al. 1985; Jenkins et al. 1998; Springel et al. 2005), or from (semi-)analytically constructed dark matter halo trees (e.g. Press & Schechter 1974; Kauffmann & White 1993; Lacey & Cole 1994; Somerville & Kolatt 1999; Sheth et al. 2001; Neistein & Dekel 2008). In the suite of cosmological simulations centered around the MR project, the dark matter simulation was performed with versions of the cosmological simulation code Gadget (Springel et al. 2005). The suite of simulations consist of (1) a 2160^3 particles simulation with particle mass $8.6 \times 10^8 h^{-1} M_\odot$ and periodic box length of $500 h^{-1}$ Mpc (Springel et al. 2005), (2) a 2160^3 particles simulation with mass $6.9 \times 10^6 h^{-1} M_\odot$ and periodic box length of $100 h^{-1}$ Mpc (the Millennium-II (MS-II); Boylan-Kolchin et al. 2009), and (3) a 6720^3 particles simulation with mass $6.2 \times 10^9 h^{-1} M_\odot$ and periodic box length of $3 h^{-1}$ Gpc (the Millennium-XXL (MXXL); Angulo et al. 2012). All simulations follow the gravitational growth as traced by these particles from $z = 127$ to 0 in a Λ CDM cosmology ($\Omega_m = 0.25$, $\Omega_\Lambda = 0.75$, $h = 0.73$, $n = 1$, $\sigma_8 = 0.9$) most consistent with the Wilkinson Microwave Anisotropy Probe (WMAP) year 1 data (Spergel et al. 2003). The dark matter particle distributions were stored at 64 discrete epochs ('snapshots').

2.1.1 Scaling of cosmological parameters

The suite of MR simulations were performed using the now disfavored WMAP1 cosmology. While the lower value of σ_8 preferred by the more recent WMAP7 data will cause the growth of dark matter structure to be delayed with respect to a WMAP1 cosmology, its effect on galaxy formation models is less straightforward to infer. Running simulations with multiple cosmologies is a time-consuming process. Instead, the MRObs project uses a recent technique introduced by Angulo & White (2010) in which the output from a cosmological N -body simulation in one cosmology (e.g., WMAP1) can be scaled to represent the growth of structure in another cosmology (e.g., WMAP7). Tests comparing direct N -body simulations done in two cosmologies with a simulation that was scaled from one to another cosmology show that power spectra are reproduced to better than 3% at all scales. In the MRObs the technique is applied to halo catalogues. Properties such as mass, concentration, velocity dispersion and spin are scaled are reproduced at about the 10% level or better (Angulo & White 2010) (see also Ruiz et al. 2011). Guo et al. (2012) give the properties of semi-analytic galaxies in the MR and MR-II scaled to the WMAP7 cosmology.

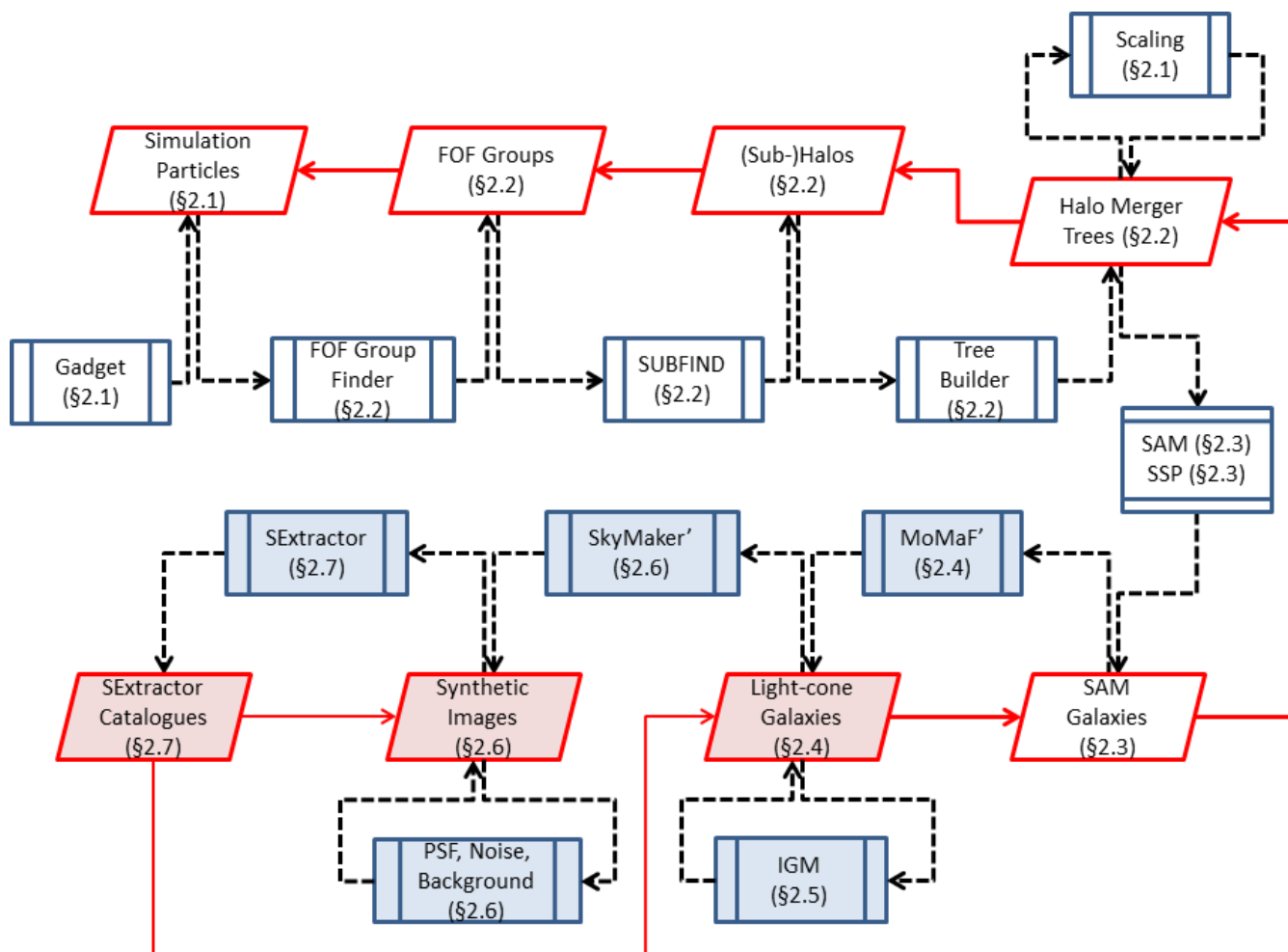


Figure 1. Schematic overview of the Millennium Run Observatory workflow. The blue rectangles indicate an action, while the red tilted rectangles represent data products that in each step can be linked to products elsewhere along the chain. Thick arrows indicate that there are direct links between data products, while thin arrows indicate that indirect links can be made using cross-correlation. Dashed lines link products to actions from which they result, or by which they are used. Shaded rectangles indicate products or actions that have been updated or are introduced in this paper for the first time. The workflow starts with an N -body dark-matter-only simulation (see §2.1). Dark matter particles are grouped together using a friends-of-friends group finder and decomposed into halos and sub-halos using a halo-finder algorithm (see §2.2). This results in positions, velocities, spin vectors and masses of dark matter halos in an evolving Λ CDM universe. A dark matter halo merger tree is constructed and stored in a database. Optionally, a scaling of the cosmological parameters can be applied to the halo merger tree (see §2.1.1). The merger tree forms the backbone for a semi-analytic model of galaxy formation that tracks the growth of galaxies inside halos based on simple recipes for, e.g., gas cooling, star formation, supernova and AGN heating, gas stripping, and merging between galaxies (see §2.3). In each time step or snapshot, the resulting physical properties of each galaxy in the semi-analytic galaxy population are used to select appropriate stellar population templates from a library of spectral energy distributions to model the rest-frame, dust-attenuated spectra or colours of each galaxy (see §2.3.2). A pencil beam-shaped ‘lightcone’ is carved out through the simulation volume using a modified version of the code MoMaF, selecting only galaxies from those snapshots that correspond to the cosmic time at the co-moving distances along the line-of-sight in the observer’s frame of reference (see §2.4). Multi-band apparent magnitudes are calculated and corrected for absorption by neutral hydrogen in the intergalactic medium (see §2.5). This lightcone is then projected onto a plane giving virtual sky positions for each galaxy in terms of right ascension and declination. The positions, shapes, sizes and observed-frame apparent magnitudes are used to build a ‘perfect’ pre-observation image of the sky using a modified version of SkyMaker (see §2.6). The perfect image is fed into the telescope simulator that applies a detector model (pixel scale, readout noise, dark current, sensitivity, gain), a sky background model, PSF convolution, and Poissonian object and sky noise for a particular survey description (see §2.6.3). The MROBs produces a realistic, synthetic telescope image in `.fits` format for further scientific analysis. Source Extractor is run on the simulated image and the output catalogs can be analyzed analogous to the catalogs constructed from real observations (see §2.7).

2.2 Dark matter halos

The MR simulations output the dark matter phase-space distribution at 61 different epochs at $z < 60$. The spacing between these outputs is roughly equal in the log of the expansion factor, specifically, ≈ 300 Myr for $z < 2$ and ≈ 100 Myr for $z > 6$. In each of these snapshots, DM haloes are found using a FOF algorithm

(Davis et al. 1985) with a linking length parameter equal to one fifth of the mean inter-particle separation. Within each FOF halo, self-bound substructures are identified using the SubFind algorithm (Springel et al. 2001).

For each subhalo, at each output time, a unique descendant in subsequent snapshots is assigned as the subhalo which contains the majority of the most bound particles (slightly different definitions

have been used among the different Millennium simulations). Finally, these pointers are arranged in a tree-like data structure which allows to access the full mass evolution of a given object across time. This structure – a halo merger tree – represents the backbone and starting point for our post-processing simulations of galaxy formation.

2.3 Synthetic galaxy catalogues

2.3.1 Semi-analytical galaxy formation models

The N-body simulations used in the MRObs follow dark matter particles only. To add predictions about the baryonic content of the model universe, we rely on an approach that generally is referred to as semi-analytical modelling (SAM) (e.g. White & Frenk 1991; Kauffmann et al. 1993; Cole et al. 1994; Kauffmann et al. 1999; Somerville & Primack 1999; Kauffmann & Haehnelt 2000; Somerville et al. 2001; Springel et al. 2001; Hatton et al. 2003; Kang et al. 2005; Cattaneo et al. 2005, 2006; De Lucia & Blaizot 2007; Monaco et al. 2007; Guo et al. 2011; Somerville et al. 2012, and references therein). Using simplified descriptions (‘recipe’) for the baryonic physics, these models follow the evolution of the galaxies within the skeleton provided by dark matter halo merging trees defined in the previous steps. These recipes include gas cooling, star formation, reionization heating, supernova feedback, mergers, black hole growth, metal enrichment and feedback from active galactic nuclei. The recipes are constrained by local observations and by physical insight.

This technique is much less computationally expensive than adding full hydrodynamics to the basic simulations. Once the backbone formed by the dark matter structure has been established, the semi-analytic modeling of the galaxies can be repeated many times in order to find the recipes and parameters that are required to match the observations.

The MRDB (Lemson & Virgo Consortium 2006) contains galaxy catalogues from two SAMs, L-GALAXIES, created at the Max-Planck-Institute for Astrophysics in Garching (Springel et al. 2001; Croton et al. 2006; De Lucia & Blaizot 2007; Bertone et al. 2007; Guo et al. 2011), and GALFORM, created by the University of Durham (Cole et al. 2000; Benson et al. 2003; Baugh et al. 2005; Bower et al. 2006). Compared to earlier models, also stored in the MRObs, the latest version of the Munich model by Guo et al. (2011) that we focus on here, includes improved prescriptions for supernova feedback, gas stripping, galaxy merging, and bulge formation (see Croton et al. 2006; De Lucia & Blaizot 2007; Bertone et al. 2007; Guo et al. 2011; Henriques et al. 2012, for successive versions of the Munich model applied to the MR). The output of the SAM is stored for each of the 64 snapshots, thus sampling the evolution of the galaxy population every few 100 Myr. The SAM calculations, however, are computed on a finer grid consisting of 20 steps of about 10 Myr each between each pair of snapshots. This ensures that the properties of galaxies are modeled on time-scales appropriate for a wide range of star formation histories, including brief bursts of star formation that may happen in between snapshots.

The galaxies resulting from the semi-analytic model naturally span a wide variety in star formation histories (SFHs), corresponding to the different gas accretion and merger histories of individual galaxies. The relational database of the MRObs allows us to reconstruct these SFHs in great detail. It is important to keep in mind the distinction between the SFH of the galaxy that forms the main branch in a galaxy merger tree, and that of the stars in all the pro-

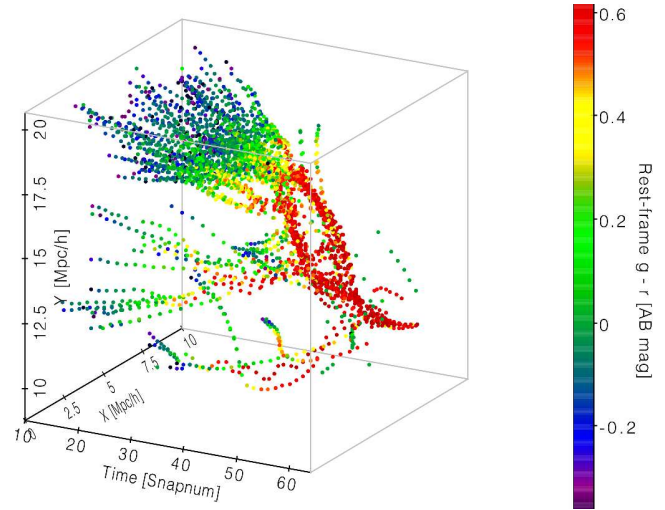


Figure 2. The merger history of a single galaxy selected from the MR. The dark matter halo properties stored in a database are used as the backbone for a semi-analytic model of galaxy formation that tracks the growth of galaxies inside halos based on simple recipes for, e.g., gas cooling, star formation, supernova and AGN heating, gas stripping, and merging between galaxies. In each time step or snapshot of the simulation, the resulting physical properties of each galaxy in the semi-analytic galaxy are used to select appropriate stellar population templates from a library of spectral energy distributions to model the rest-frame spectra or colours of each galaxy. In the example shown here, the colour coding indicates the rest-frame $(g' - r')$ colour of all the galaxies that are part of the merger tree of a single galaxy selected in the simulation snapshot 63 ($z = 0$), starting from 10 ($z \approx 12$). The other two axes show the 2D positions of these galaxies in the simulations volume.

genitors of a descendant identified at some snapshot. As shown by De Lucia & Blaizot (2007) this typically results in large differences between the time it took for the stellar mass to be formed (‘formation time’) and the time it took for that mass to assemble into a single galaxy (‘assembly time’). An example is shown in Fig. 2, showing the stellar populations of all the different branches that form the merger tree of a single galaxy at $z = 0$. When observers study the star formation history of a particular galaxy selected at some redshift, they do thus not necessarily study the SFH of a single galaxy, but rather the SFH of all its progenitors (weighted by stellar mass).

Similar to real galaxies, galaxies in the MRObs span a very large range in SFHs. In Fig. 3 we show the average SFHs for star-forming and quiescent galaxies in the MRObs. These SFHs were determined by summing the SFRs of all the progenitors of 100 galaxies selected at $z \approx 2$. For systems having SFRs of $>10 M_{\odot} \text{ yr}^{-1}$ and $M_{*} \sim 10^{10} M_{\odot}$ (e.g., similar to Lyman Break Galaxies, LBGs), the SFHs are rising (blue line in Fig. 3), roughly as derived from observations of LBGs (Papovich et al. 2011). For systems having SFRs of $<10 M_{\odot} \text{ yr}^{-1}$ and $M_{*} \sim 10^{11} M_{\odot}$ (e.g., similar to Distant Red Galaxies, DRGs), the average SFH rapidly declines after $z \sim 5$ (red line) analogous to the best-fit SFHs of DRGs observed (e.g. Kriek et al. 2006).

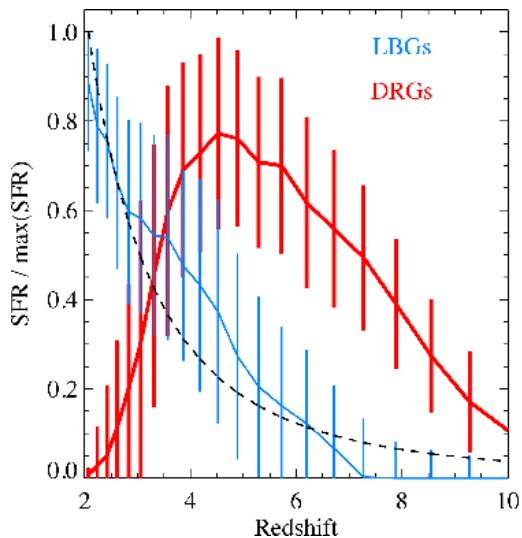


Figure 3. The average SFHs of star-forming and quiescent galaxies identified in the SAMs at $z \approx 2$. The LBG-like systems (blue line) show a rising SFH, analogous to that derived from observations (Papovich et al. 2011, dashed line). DRG-like systems have SFHs that sharply decline after $z \approx 5$.

2.3.2 Multi-wavelength model predictions

SAMs predict physical properties of galaxies, such as their stellar masses, ages, metallicities, and gas content. One common way of testing the models is to compare them to the same physical properties derived from the SEDs of observed galaxies. At the least, this approach depends on having well-established measuring techniques and accurate stellar population synthesis models (see Tinsley 1980). In practice, this sort of analysis typically includes numerous assumptions, and certain features of the galaxies can never be recovered from the observations in full (e.g., their exact star formation history or dust attenuation). In the MRObs the application of stellar population synthesis models and dust recipes allow one to make detailed spectro-photometric predictions for the model galaxies by adding up synthetic spectra corresponding to the different generations of stars that these galaxies consist of at any moment. The great predictive power of SAMs in terms of the observable, photometric properties of galaxies is in large part based on the spectral synthesis modeling of the stellar populations being formed in the semi-analytic model galaxies according to their SFRs at any given time (see Fig. 2 for an example of a typical galaxy).

The predicted multi-wavelength properties of galaxies depend on the spectral synthesis model used. These models are currently still affected by gaps in our understanding of stellar evolution (e.g., see Conroy et al. 2009), preventing us from making unambiguous predictions for the main galaxy observables. Two well-known synthesis models implemented in the MRObs are those by Bruzual & Charlot (2003, ‘BC03’) and by Maraston (2005, ‘M05’). These models are illustrated in Fig. 4, where we show the observed $K-4.5\mu\text{m}$ vs. $B-K$ colour-colour diagram for galaxies at $z \sim 2$ in our simulations. The M05 model shown right predicts significantly redder colours compared to the BC03 model shown left, especially for galaxies between 1 and 2 Gyr in age (for discussion, see Tonini et al. 2010; Henriques et al. 2011, and references therein).

We model the effect of dust on the predicted colours and magnitudes using the dust treatment recipe detailed in Guo & White (2009) (see also De Lucia & Blaizot 2007; Kitzbichler & White

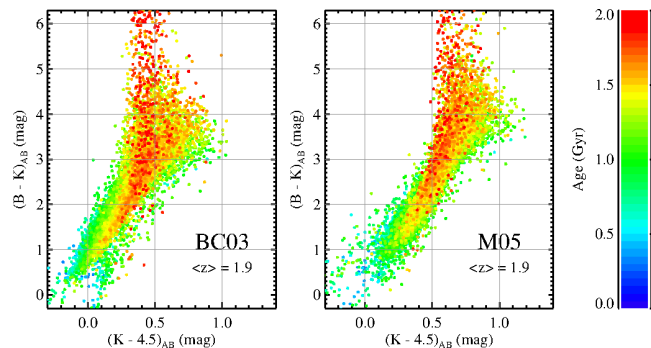


Figure 4. The choice of stellar population synthesis model affects the colour distributions of galaxies. We illustrate this by showing the optical-infrared colour-colour diagrams for galaxies at $z \sim 1.9$ selected from the lightcones modeled using BC03 (Bruzual & Charlot 2003, left panel) and using M05 (Maraston 2005, right panel). Galaxies are colour-coded according to their mass-weighted age (see legend on the right). See also Maraston et al. (2006, Fig. 2 in that paper). The MRObs offers the choice between different spectral synthesis models.

2007; Guo et al. 2011; Henriques et al. 2012), and we note that in calculating the extinctions, a random inclination was assigned to every galaxy to determine the extinction relative to the face-on value (assuming a slab geometry). It is important to note that the dust modeling in semi-analytic models is currently performed in a highly simplistic manner. Even though models have shown to be fairly successful in reproducing the overall colours of the evolving galaxy population in some bands, a more realistic treatment of the effects of dust could easily alter the spectral energy distributions of certain galaxies at any given time significantly.

The significant uncertainties in the stellar population synthesis models and the dust modeling techniques limit us in producing accurate models of the real universe. For the same reasons, however, they also limit our ability to derive exact physical quantities from real observations. At the very least, the MRObs will thus allow one to test the accuracy of current techniques designed to extract physical quantities from a given set of broadband magnitudes. In the future, the highly modular approach of the MRObs (see Fig. 1) will make it straightforward to add alternative or improved models.

In the current version of the MRObs, the SFHs, stellar synthesis models, and dust extinction models mentioned above are used to generate multi-wavelength filter catalogs (see Henriques et al. 2011, 2012). These catalogs cover the FUV to the mid-IR as observed by major telescopes and instruments (Table 1). The filter bandpasses are illustrated in Fig. 5.

2.4 Lightcone construction

The snapshots of data (in time or in redshift) that are produced by numerical simulations present an idealized view of the evolving universe that is different from data resulting from observations of the extra-galactic sky. In order to allow for more realistic and direct comparisons between the model predictions and observations, we construct so-called ‘lightcones’ in which galaxies that were simulated at discrete snapshots are re-arranged in order to mimic the relation between the distance along an observer’s line of sight and cosmic time as accurately as possible (e.g., see Hamana et al. 2001; Blaizot et al. 2005; Kitzbichler & White 2007; Sousbie et al. 2008; Guo & White 2009; Overzier et al. 2009a; Teyssier et al. 2009; Carlson & White 2010; Henriques et al. 2012).

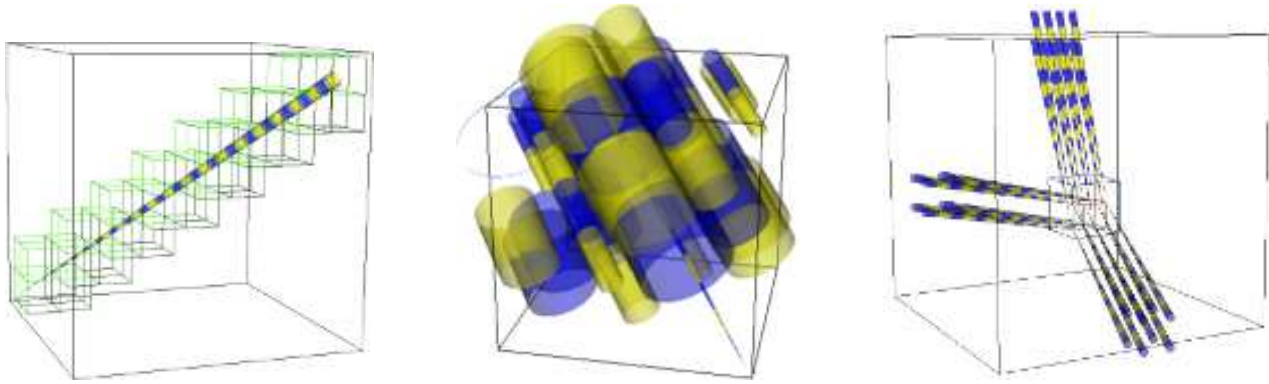


Figure 6. The construction of the lightcones. *Left panel:* The lightcone is constructed by replicating the simulation box until the co-moving distance corresponding to the desired limiting redshift is reached. In this example, the original co-moving size of the MR simulation is extended from 500 Mpc/h to ~ 7000 Mpc/h, corresponding to $z \approx 10$ for $h = 0.73$. A conical volume is carved out from the volume that has now been expanded through the box replication process, and galaxies are selected from the overlap between the cone and the replicated volume. In order to model the relation between co-moving distance and redshift, at any point along the cone galaxies are selected only from that snapshot that is closest in redshift to the one corresponding to the co-moving distance along the line-of-sight. We do not interpolate over physical properties of the galaxies (they are assumed to be relatively constant between two consecutive snapshots), but apparent magnitudes and colours are interpolated, to make sure that galaxies have the right values for their redshifts. *Middle panel:* The starting position and orientation of the lightcone through the simulation box can be chosen such that the entire replicated volume can be constructed out of conical segments (drawn in blue and yellow) drawn from the original volume without passing through any region twice. Different ‘views’ of the simulated universe can be created by changing the starting points or orientations of the cones. Narrow pencil beams can be constructed out to very high redshift without replications, while very wide-field surveys can be made by keeping the limiting redshift low. Much larger volume surveys can be generated if the scientific application of interest allows some degree of replication. *Right panel:* Multiple lightcones can be extracted from the simulations box by choosing different starting positions (the position of the observer, $z = 0$) and orientations (specified by the two angles θ, ϕ). The 24 ‘field’ lightcones from Henriques et al. (2012) each with an opening angle of $1.4^\circ \times 1.4^\circ$ are indicated.

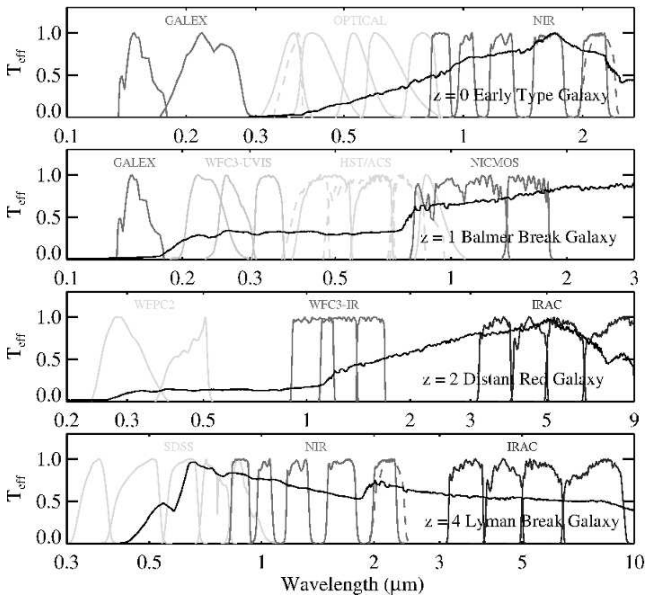


Figure 5. Examples of filter sets currently available in the MROBs: space-based UV (GALEX, HST WFC3-UVIS), ground-based optical (Johnson, SDSS, VIMOS), space-based optical (HST WFC2, ACS), ground-based near-IR (Johnson, VISTA), space-based near-IR (HST NICMOS, WFC3-IR), and mid-IR (Spitzer/IRAC). Typical model galaxy spectra at $z = 0$, $z = 1$, $z = 2$, and $z = 4$ are shown for reference (black curves).

In this paper we use lightcones introduced in Henriques et al. (2012), to which we add structural properties, and a set of new lightcones pointed at specific objects. These lightcones were built using a version of the Mock Map Facility (MoMaF) code of

Blaizot et al. (2005). Because of its importance to the MROBs, here we give a short review of the technique, and describe a use of MoMaF that allows us to create lightcones aimed at specific objects of interest in the simulations and which is specially developed for the MROBs.

2.4.1 Summary of our lightcone method

The MR predicts the detailed properties of the dark matter and the galaxies it contains for a closely spaced set of snapshots that are sufficient to compare with observations from $z = 0$ to the highest redshifts currently observed. In principle the simulations box probes a sufficiently large volume to construct large pencil beam surveys. For example, the total simulations volume of $(500 h^{-1} \text{ Mpc})^3$ is equivalent to that probed in a pencil beam survey out to $z = 10$ and measuring 4 square degrees on the sky. On the other hand, the co-moving distance to $z = 10$ of $\sim 7,000 h^{-1} \text{ Mpc}$ is much larger than the side of the simulations box of $500 h^{-1} \text{ Mpc}$ ($900 h^{-1} \text{ Mpc}$ when taking the diagonal through the box).

Blaizot et al. (2005) suggested ‘replicating’ the simulations box along an artificial observer’s line of sight until the maximum co-moving distance desired is reached, and then extracting a conical pencil beam out of the enlarged volume. They explain that care must be taken to avoid ‘perspective effects’ caused by replication of the same part of the universe in certain directions. Whereas Blaizot et al. (2005) solve this by adding random rotations and translations of the boxes, thereby introducing discontinuities in the galaxy distribution, Kitzbichler & White (2007) showed that for certain orientations of the lightcones through the MR box and for a small enough opening angle of the cone, the lightcone can be constructed without passing through any region of the simulations twice (or at least ensuring that copies are widely separated in red-

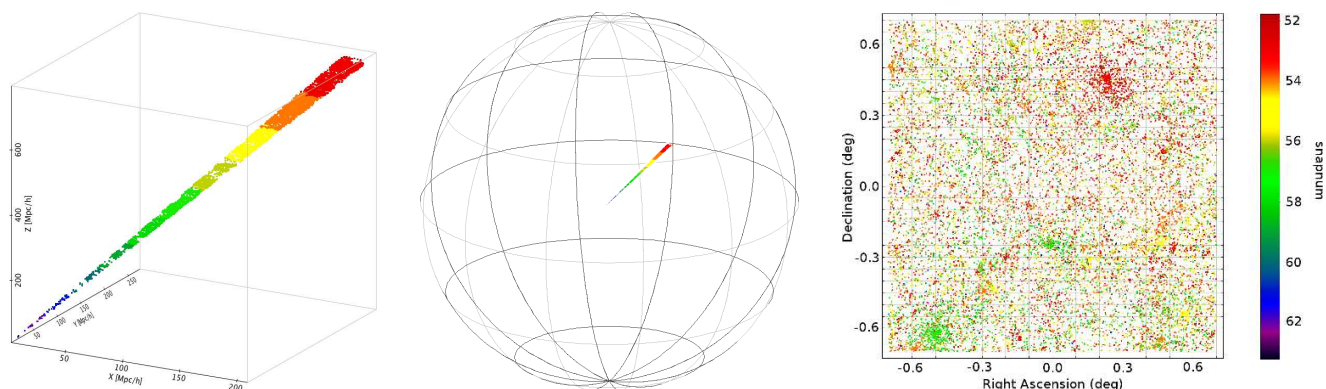


Figure 7. Lightcone construction further explained. *Left panel:* The lightcone in the expanded co-moving coordinate frame. *Middle panel:* Projection of the lightcone onto a virtual celestial sphere. *Right panel:* Galaxies in the lightcone as seen projected on the sky. The colour bar on the right illustrates which particular snapshot was used to populate each of the different sections along the lightcone. For clarity, we only plot the lightcones out to $z \approx 0.3$ (snapnum = 52). In reality our lightcones extend to beyond $z = 10$ following the same procedure.

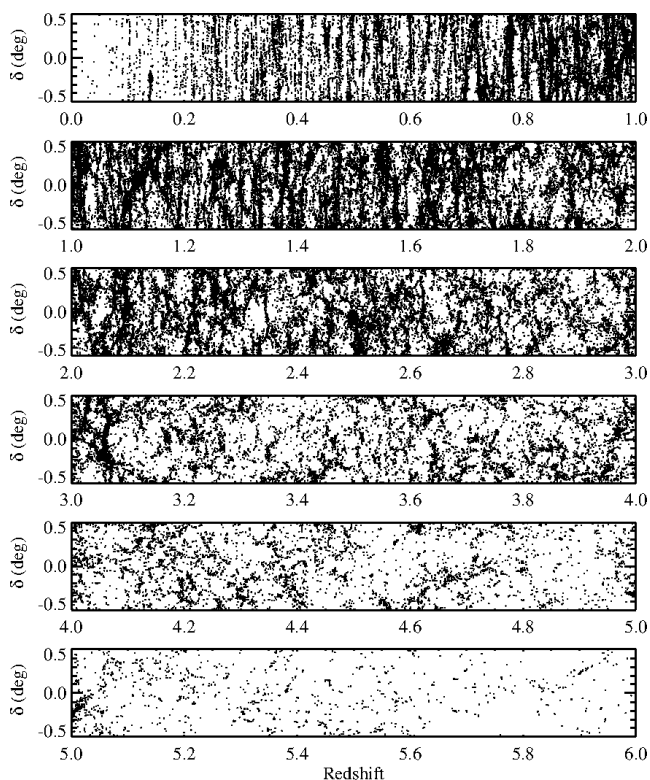


Figure 8. Detail of a lightcone from Henriques et al. (2012) shown in the redshift versus declination plane. Galaxies plotted have SDSS z' -band magnitudes of < 26.5 (AB). The range in right ascension was limited to ± 0.1 deg for easier viewing.

shift if replication occurs). It is the latter method that we use for all pencil-beam light cones in the MROBs.

We illustrate the box-replication process in Fig. 6. In the panel on the left, a virtual lightcone is drawn in a much enlarged MR volume constructed using the box replication method. The opening angle of the cone, its origin and angles of intersect with the original MR box are chosen such that every cone segment (indicated by the blue-yellow segments) can be extracted from the original MR volume in such a way as to almost cover the complete simulation

volume and without passing through any region of the box twice (as illustrated in the middle panel). Many pencil beam surveys can be constructed from the MR by changing the angles or the origin of the cone (right panel).

Besides these geometric considerations, one must take special care that each galaxy is seen at the evolutionary phase and with the photometric properties corresponding to its redshift along the lightcone. In the MR, snapshots are separated by ~ 100 – 400 Myr, meaning that the evolving galaxy population is sampled at fairly frequent intervals out to very high redshifts. Fig. 7 illustrates how we connect data from many individual snapshots to obtain an evolving galaxy population as a function of co-moving distance (or redshift) along the lightcone. Each section consists of those galaxies having redshifts $(z_i + z_{i+1})/2 > z > (z_i + z_{i-1})/2$, where z_i is the redshift corresponding to snapshot i . The physical properties that these galaxies have are then also those they have in snapshot i . Because the large-scale structure does not evolve rapidly between snapshots, it is safe to neglect any changes occurring in the distributions of galaxies. However, due to the relatively sparse number of snapshots, especially at very high redshifts, one has to be aware of the fact that there may be discontinuities or ‘jumps’ in the absolute numbers of sources as one moves from one lightcone section to the next. The physical properties of the galaxies can also fluctuate heavily between snapshots, but as long as one is interested in the evolution of the global population this can be safely ignored (Kitzbichler & White 2007). However, in order to ensure that ‘observed’ galaxy properties are correctly related to redshift we perform small interpolations of the observed-frame magnitudes, shifting each galaxy in both redshift and luminosity distance from the snapshot corresponding to redshift z_i to the redshift at which it actually appears on the lightcone (Blaizot et al. 2005; Kitzbichler & White 2007). In addition to this step, we make corrections to the observed magnitudes due to absorption by the IGM (see §2.5).

The final step required is to project the cone onto a virtual sky seen by a fictitious observer placed at the center of the celestial sphere (middle panel of Fig. 7). It is now straightforward to assign WCS coordinates (right ascension and declination) to every object in the cone (see Kitzbichler & White 2007). The projected large-scale structure can be seen in the sky distribution of galaxies plotted in the right-hand panel of Fig. 7. Now that we know both the sky coordinates and the redshifts to every object along the

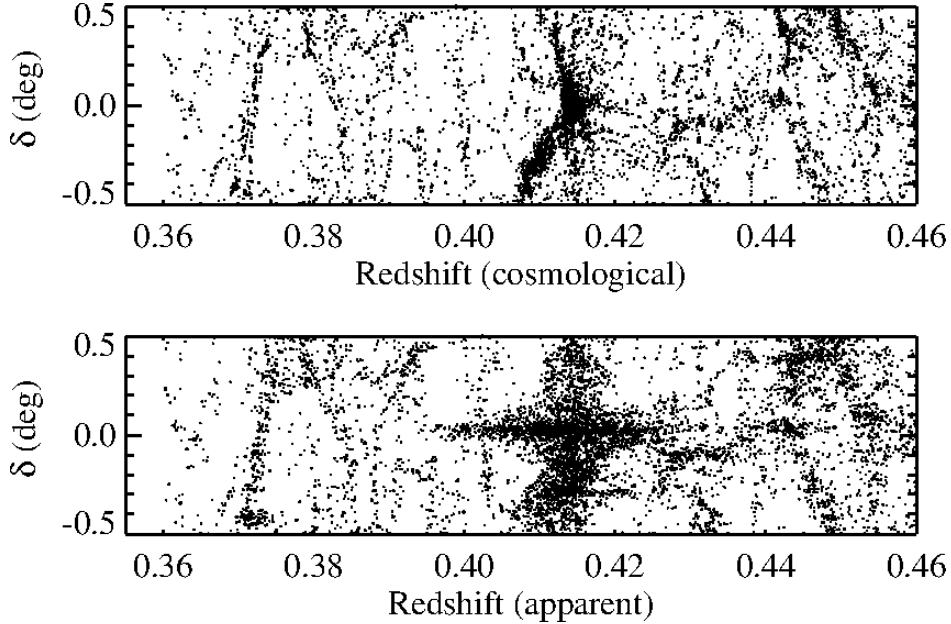


Figure 9. The effects of galaxy peculiar velocities on the apparent redshifts of galaxies in the lightcone. The top panel shows declination vs. the geometric or cosmological redshift for galaxies in and near a massive galaxy cluster at $z \approx 0.4$. The bottom panel shows the redshift-space distortions an observer would see due to the peculiar velocities of galaxies moving through the gravitational potential well of the cluster.

lightcone, we can show the details of the large scale structure that would be probed in a deep pencil beam survey as it would appear in a large galaxy redshift survey out to $z \approx 8$. In Fig. 8 we plot the redshifts of objects versus their declination on the sky for one of the Henriques et al. (2012) lightcones. Points represent galaxies having z' -band magnitudes brighter than 26.5 (AB) mag.

2.4.2 Aiming at a specific object

We have made a small modification to the MOMAF code that allows for the construction of lightcones not only in arbitrary directions as described above, but to also ‘aim’ a lightcone such that it crosses through a specific point of the MR box at a specific co-moving distance (or redshift) from the origin. This new technique enables us to model observations toward specific objects or regions by choosing a location within the simulations volume at one redshift and ‘observing’ it within a lightcone with origin at another redshift. Obvious uses of this technique are to study the appearance of a particular galaxy cluster selected at $z = 0$ and observed at $z = 1$, or to study the $z = 0$ descendant of a halo (or galaxy) selected at $z = 6$. It is important to take into account the peculiar velocities of galaxies when constructing the lightcones as they can heavily distort the observed redshift distributions, especially in the vicinity of massive objects such as galaxy clusters (see Fig. 9).

The MRDB allows one great flexibility in selecting such targets, and even allows one to define the complete geometry of the light cone in a single SQL query. Our new lightcone aiming technique thus greatly enhances the application of the MR to numerous new problems. Examples related to galaxy clusters will be shown in §4.2.

2.4.3 Inclinations and position angles

One of the unique features and key science drivers of the MRObs is that it aims to produce detailed predictions for the observed galaxy population without having to make assumptions that are not supported or naturally accounted for by the model. The SAMs included in the MRObs allow us not only to predict morphologies and sizes of galaxies, but also their inclinations and position angles as seen by a virtual observer. The latter are derived from the orientation of the galaxy as defined by the angular momentum vector of its stellar disk. The SAM that we use here tracks the change in the total angular momentum vector of both gas and stellar disks. New gas condensing within a halo is assumed to carry the specific angular momentum of that halo. The total angular momentum change of gas disks in each time step is the sum of the change in angular momentum due to gas condensation, gas accretion and gas that is transformed into stars. The change in total angular momentum of stellar disks is given by the change in angular momentum due to gas that gets transformed into stars in each time step.

As a consequence, the SAM predicts not only the spatial positions but also the orientations of all galaxies with respect to the three-dimensional, co-moving, Cartesian coordinate system of the simulation box. From this we can then calculate the observed inclinations and position angles of each galaxy based on the angles between the line of sight of our lightcone and the simulation box. Our method ensures that the orientations of galaxies in the MRObs are, at the very least, physically motivated. This allows one to study in detail if the MR predicts any observable correlations between the orientations of galaxies, their parent halos or the large-scale structure. Such models are also suited for, e.g., conducting completeness tests as a function of inclination, for testing galaxy structure decomposition codes, and for paving the way for more elaborate, orientation-based dust screening models that may be implemented into the SAM at a later stage.

2.5 IGM absorption models

The spectra of galaxies short-ward of 1216 Å in the rest-frame are primarily affected by photoelectric absorption by the neutral hydrogen associated with damped Ly α absorbers (DLAs), Lyman Limit Systems (LLSs), optically thin systems, and resonance line scattering by the Ly α forest along the line of sight². This absorption affects the magnitudes and colours of galaxies observed in bands corresponding to these rest wavelengths. The strength and shape of this so-called ‘Lyman Break’ depend on the redshift of the source, the intrinsic source spectrum, and the distributions in redshifts and optical depths of the absorbing systems. In order to ensure that these effects are properly accounted for in the MRObs lightcones, at least in a statistical manner, we have implemented three different models for the IGM absorption. We include two models based on the recent IGM transmission calculations by Meiksin (2006, ‘MEIKSIN’) and Inoue & Iwata (2008, ‘INOUE-IWATA’) that are conveniently made available in code form by Harrison et al. (2011, `IGMtransmission`). We also include the IGM transmission model of Madau (1995, ‘MADAU’) that is still the most widely used in the literature today even though it has been shown to significantly over-predict the absorption in the 912–1216Å range compared to the updated models (e.g. Bershadsky et al. 1999; Meiksin 2006; Inoue & Iwata 2008).

For an intrinsic galaxy spectrum f_λ , the attenuated spectrum observed will be of the form $f_{\lambda,e} = f_\lambda \cdot e^{-\tau_e(\lambda)}$, where the effective optical depth of the IGM transmission function can be taken from any of the three IGM models. In Fig. 10 we show the mean transmissions for sources at different redshifts. The MADAU model implies significantly less transmission than the other models.

In the current release of the MRObs, the IGM absorption correction is calculated only after the filter magnitudes are computed. We approximate the spectral shape within the filter response with that of a 100 Myr old, continuously star-forming, solar metallicity stellar population modeled using Starburst99 (Leitherer & Heckman 1995). For most practical purposes (i.e. in the case of galaxies with significant far-UV emission from a young stellar population), this is a reasonable assumption, and we note that the same assumption is typically made by observers when interpreting the broad-band colours of high redshift dropout galaxies (e.g. Bouwens et al. 2003). In any case, the corrections do not significantly change when assuming a 3 Myr old instantaneous low-metallicity starburst model (<0.05 mag change). Although refinements to this method will become available in the MRObs in the future, users can already also apply their own IGM corrections directly on the unattenuated lightcone catalogs that we provide and then use these as the basis for their own image simulations. Because the inclusion of the IGM attenuation is so important for creating realistic mock catalogs and images in the MRObs, a brief review of the MEIKSIN, INOUE-IWATA, and MADAU modeling recipes is given in Appendix A.

2.6 Construction of the virtual telescope data

2.6.1 Galaxy models

Now that we have obtained all the necessary information pertaining to the positions, sizes, viewing angles, bulge-to-disk ratios, and IGM-corrected magnitudes across different filters, we can populate

² In our model approximations we neglect the much smaller contribution from intergalactic metals and He absorption.

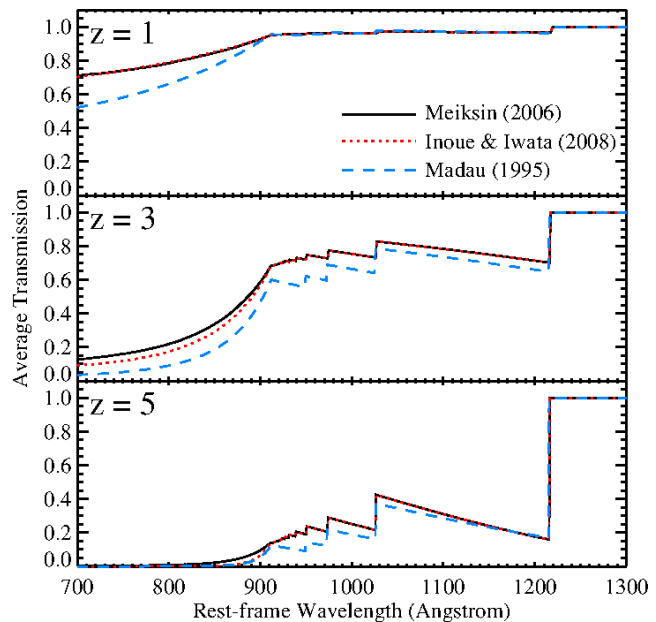


Figure 10. Attenuation of the UV continuum short-ward of Ly α due to neutral hydrogen along the line of sight, which affects the colours of high redshift galaxies. Panels show the average transmission of the IGM according to the analytic approximation given by Madau (1995, blue dashed curves), and the more recent Monte Carlo modeling techniques of Meiksin (2006, black solid curves) and Inoue & Iwata (2008, red dotted curves) for example galaxies at $z = 1$ (top panel), $z = 3$ (middle panel), and $z = 5$ (bottom panel). The MRObs offers the choice between the different IGM implementations.

simulated images with galaxies. We follow a two-step process. First we simulate noise-free galaxy profiles projected onto a 2D image plane at very high pixel resolution using a modified version³ of Skymaker (Bertin 2009). We will refer to the result of this process as the ‘perfect’ or ‘pre-observation’ image. Once the perfect image has been made, it is straightforward to apply all the observational effects such as the PSF, binning, sky background, and noise for any type of observation. This last step is done using our own custom code⁴.

In line with the Guo et al. (2011) semi-analytic predictions, galaxies in the MRObs are composed of an exponential profile for the disk (D) and a De Vaucouleurs profile (S) for the bulge (if any), each having a surface brightness profile $\mu(R)$ in mag arcsec⁻² given by:

$$\begin{aligned} \mu_S(R) &= m - 2.5 \log_{10}(B/T) + 8.3268(R/R_e)^{1/4} \\ &+ 5 \log_{10}(R_e) - 4.9384 \end{aligned} \quad (1)$$

$$\begin{aligned} \mu_D(R) &= m - 2.5 \log_{10}(1 - B/T) \\ &+ 1.0857(R/R_h) + 5 \log_{10}(R_h) + 1.9955, \end{aligned} \quad (2)$$

where m is the total magnitude (mag), B/T is the bulge-to-total ratio, R_e is the bulge half-light radius (arcsec), and R_h the disk

³ We optimized Skymaker for dealing with very large input lists in .csv format provided by the MRDB, and for generating extremely large images.

⁴ Although Skymaker was specifically designed to handle point spread function convolution, sky backgrounds, and simulating detector noise, for various practical reasons we do not currently make use of this functionality but use our own custom IDL and Python codes for these steps of the simulation.

scale height (arcsec). Skymaker builds these profiles as elliptical shapes at pixel position $x' = x - x_c$, $y' = y - y_c$ projected on the sky with position angle θ and inclination ϕ according to (see Bertin & Arnouts 1996):

$$C_{XX} \cdot x'^2 + C_{YY} \cdot y'^2 + C_{XY} \cdot x' y' = R^2, \quad (3)$$

such that the algorithm for calculating the projected light profiles for disks and bulges becomes:

$$\begin{aligned} I_D[x', y'] &\propto e^{-(C_{XX} \cdot x'^2 + C_{YY} \cdot y'^2 + C_{XY} \cdot x' y')^{1/2}} \\ I_S[x', y'] &\propto e^{-7.6693(C_{XX} \cdot x'^2 + C_{YY} \cdot y'^2 + C_{XY} \cdot x' y')^{1/8}}, \end{aligned} \quad (4)$$

with

$$\begin{aligned} C_{XX} &= \frac{\cos^2(\theta)}{A^2} + \frac{\sin^2(\theta)}{B^2} \\ C_{YY} &= \frac{\sin^2(\theta)}{A^2} + \frac{\cos^2(\theta)}{B^2} \\ C_{XY} &= 2 \cos(\theta) \sin(\theta) \left(\frac{1}{A^2} - \frac{1}{B^2} \right). \end{aligned}$$

A and B are the projected major and minor axes, with $A = R_h$ for disks and $A = R_e$ for bulges, and $B = A \cos(\phi)$ with $\cos(\phi)$ the projected aspect ratio of the system.

Our modified version of Skymaker performs this process efficiently for typical MROBs simulations that are based on lightcones containing several millions of galaxies per square degree. An example of the ‘perfect image’ produced is shown in the left panel of Fig. 11, where the white shapes indicate the simulated galaxy images. The corresponding final (‘noisy’) telescope image produced following the process detailed below is shown in the middle panel.

2.6.2 Input parameters: positions, magnitudes, inclinations, orientations, sizes, and bulge-to-disk ratios

The center positions of all objects in the image plane are determined from the right ascension and declination relative to the lightcone centres and the pixel scale of the desired instrument. Inclinations and position angles are uniquely determined from the angular momentum vector of the stellar disks relative to the orientation direction of the lightcones through the MR volume (Fig. 6). Angular sizes are determined from the physical size and the diameter distance, D_A , at the redshift of each source in the lightcone.

We list the specific parameters required by Skymaker for simulating each galaxy, and give a brief explanation of how this parameter follows from our models.

- x_c, y_c : The source position in image pixel coordinates. This position is defined by the sky coordinates of a galaxy in the lightcones, the desired pixel scale of the image, the field of view, and the position of the image center relative to the lightcone center.

- m : The total apparent (AB) magnitude of the source in the desired filter. This magnitude includes the attenuation by dust as well as the IGM absorption.

- B/T : The bulge-to-total ratio of the source. This parameter, for which we take the ratio of the fluxes predicted for the bulge and total in each filter, is needed for assigning magnitudes to the bulge ($m_b = m - 2.5 \log_{10}(B/T)$) and disk ($m_d = m - 2.5 \log_{10}(1 - B/T)$) components.

- $R_{h,disk}$: The scaleheight of the disk in arcseconds. This is defined by `stellardiskradius/3DA`, with

`stellardiskradius` taken from the `Guo2010a..MR table5` in the MRDB and is in units of kpc.

- $R_{e,bulge}$: The equivalent (or half-light) radius of the bulge measured in arcseconds. This is calculated as `bulgesize/DA`, where `bulgesize` is taken from the `Guo2010a..MR table` and is in units of kpc.

- $\cos(\phi_{disk})$: The projected aspect ratio of the disk that is uniquely determined by the angles of intersection of the lightcone with the MR volume and the intrinsic spin axis of the galaxy stellar disk.

- θ_{disk} : The position angle of the disk, defined by the angles of intersection of the lightcone with the MR volume and the intrinsic spin axis of the galaxy stellar disk.

- $\cos(\phi_{bulge})$: The projected aspect ratio of the bulge. Because all bulges in Guo et al. (2011) are spherical, we set this value to 1.0.

- θ_{bulge} : The projected aspect ratio of the bulge. Because all bulges in Guo et al. (2011) are spherical, we set this value to 0.0.

2.6.3 The virtual telescope model (sky, PSF, noise, and all that)

The MROBs produces realistic telescope data by applying an ‘observation description’ (OD) to the perfect image created in the previous step. The OD consists of a set of instructions that completely defines a particular observation to be mimicked, e.g., telescope, detector, filter, exposure time, number of sub-exposures, dither strategy, and sky conditions. Although the exact modeling method may vary depending on the details of a specific instrument or survey, here we list the basic observational effects typically being added in sequence:

- (1) The first step is to scale the perfect image populated by our bulge+disk surface brightness simulations to their proper fluxes measured in detector electrons by multiplying the models in Eq. 4 by the factor

$$F_{e-} = 10^{-0.4(m_{AB} + ZP)} \cdot T_{\text{exp}} \cdot G / \sum_{i \in S} \sum_{j \in S} I[x'_i, y'_j], \quad (5)$$

where m_{AB} is the AB magnitude of the disk/bulge, ZP is the zero-point in AB magnitudes that gives a detector count rate of 1 ADU s^{-1} , T_{exp} the image exposure time in seconds, G is the detector gain in $e^- \text{ADU}^{-1}$, and x'_i and y'_j are the coordinates of pixel i, j belonging to each source.

- (2) We add a sky background. The value of the background is usually kept constant across the field (we use gnomonic projections) based on the average conditions at a particular site or telescope, or is based on the sky background level measured in a particular survey that is being modeled.

- (3) The image is convolved with a point spread function (PSF). The PSF can have various origins: it can be taken from a PSF simulator (e.g. TinyTim in the case of HST), from (a stack of) stars extracted from a fully reduced observation, or modeled with a simple function (e.g., a Gaussian).

- (4) The image is rebinned to the desired pixel scale. If the PSF is taken from an actual observation and is not available at sub-pixel resolution, the rebinning step is performed before the PSF convolution step.

- (5) Detector dark current is added to the image.

- (6) Poisson noise is calculated for each pixel value.

- (7) Gaussian-distributed readout-noise is added.

⁵ The `Guo2010a..MR table` stores the galaxy catalogue obtained by applying the SAM from Guo et al. (2011) to the MR halo merger trees.

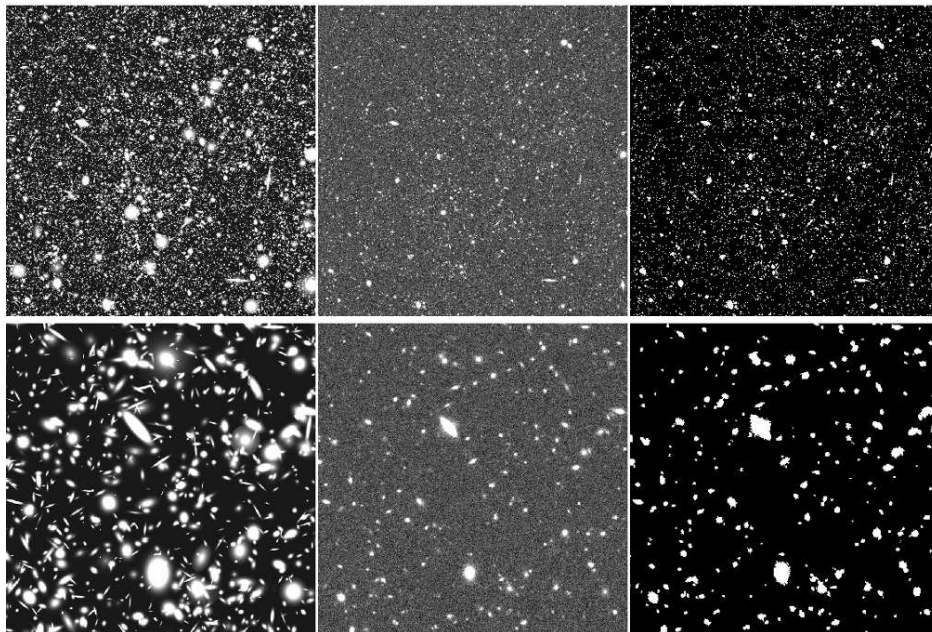


Figure 11. Single filter simulated image constructed from a lightcone. *Left panels:* The ‘perfect’ image modeled using Skymaker. Galaxies consisting of disks and bulges are placed at the proper position, inclination, orientation, brightness and apparent size that are all uniquely determined by the semi-analytical model and the angles of intersection between the lightcone and the simulations volume. The only information that is not constrained by the model is the bulge shape, which we set to spherical. *Middle panels:* The perfect image as seen by our telescope simulator. Here we show a mock HST/WFC3 F160W `.fits` image having the same detector properties, point spread function, sky background, and signal-to-noise as the ERS observations (a $1'.5 \times 1'.5$ region is shown at a spatial binning of $0''.09 \text{ pixel}^{-1}$). No stars were added to this observation. *Right panels:* The SExtractor ‘segmentation’ image showing the locations and shapes of objects that were detected in the simulated image. Panels on the bottom row show a zoom of the full images shown in the top row. Although there is a good correspondence between objects seen in the simulated telescope image and objects detected by SExtractor, the perfect image that was used as the input for the image simulation contains many more sources that are too faint to be seen in the simulated image.

(8) WCS astrometry is added to the image header based on the pixel scale and the astrometric system of the lightcone.

(9) Scientific images in `.fits` format are created, optionally with corresponding background and noise maps. Complex observations having the proper noise characteristics can be created from co-adds of multiple exposures made following the same above procedures.⁶

The middle panels of Fig. 11 show a mock HST/WFC3 H_{160} -band image corresponding to the perfect image shown on the left. The mock HST image was modeled after the H_{160} -band observations of the GOODS ERS survey of Windhorst et al. (2011).

2.6.4 Galactic extinction and stars

Optionally, we apply Galactic foreground extinction to the input galaxy models by specifying the amount of reddening in units of $E(B-V)$ and assuming the Cardelli et al. (1989) attenuation curve with $R_V = 3.1$. If desired, Galactic stars can be added to the image, either based on a user-specified input distribution or based on an accurate Milky Way model (e.g., TRILEGAL; Girardi et al. 2005).

⁶ Although the original version of Skymaker is capable of simulating bleeding, blooming and saturation, we do not currently include these effects for practical purposes. However, we do release the object input lists and the ‘perfect’ images for all our simulations (§5), such that interested users can perform their own modeling of these (or other) effects.

2.7 Source extractor

With the synthetic images produced in the previous section, it is straightforward to analyze the data analogous to real observations. Sources in the images are detected by using the Source Extractor (SExtractor) software (Bertin & Arnouts 1996), which efficiently decomposes a pixel image into ‘objects’ detected at some specified threshold of flux above the image background. Photometry and other basic measurements are performed on all the detected objects yielding a source catalog corresponding to the image. The exact way in which objects are defined and how measurements are performed depend on the setting of various of the parameters in SExtractor, while the total number of objects that can be recovered from the image and the errors on their photometry largely depend on the image quality itself. The MRObs makes it convenient to test the different detection and photometry techniques available in the literature, especially because the properties of the galaxies that were used to create the mock image are exactly known (as opposed to galaxies in real observations).

We have run SExtractor on the mock HST/WFC3 H_{160} -band image shown in Fig. 11 (middle panels). Panels on the right show the SExtractor ‘segmentation image’, indicating all the objects that were detected in the mock image. While there is good correspondence between the two (nearly all objects seen in the mock image are also seen in the detection image), the perfect (input) image shown on the left contains many more galaxies, most of which are too faint to be detected in the mock observation. By cross-correlating the positions of detected objects listed in the SExtractor output catalogs with the positions of objects in the underlying light-

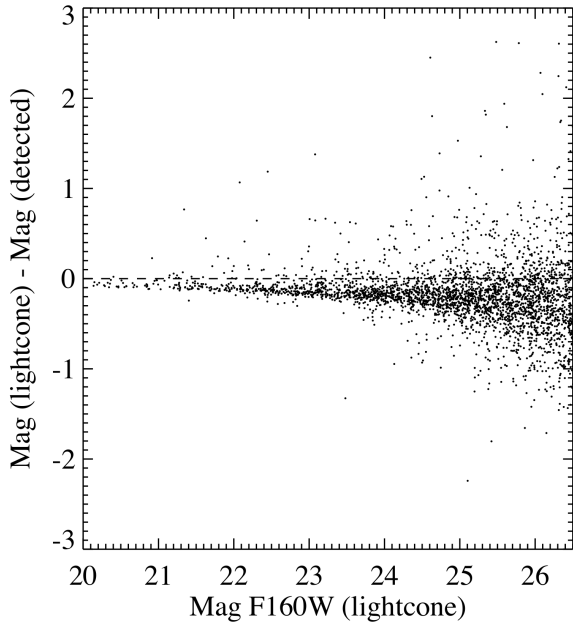


Figure 12. ‘Trumpet’ diagram showing the difference between the input magnitudes (from the MR lightcones) and the magnitudes measured by running SExtractor on a simulated HST/WFC3 H-band image.

cone (both available in the MRDB), we can find out which of the semi-analytic galaxies (identified by their `GALAXYID`) were detected in the image. This enables us to perform various diagnostic tests between measurements extracted from the synthetic observations and the corresponding intrinsic physical properties from the lightcone. One such test is to study how well the real magnitudes are recovered from the synthetic images by SExtractor. In Fig. 12 we show a so-called ‘trumpet’ diagram indicating the difference in magnitude between the ‘true’ input value and the total magnitude given by SExtractor. The test shows, quantitatively, both how the amount of flux lost due to missed light, and how the photometric scatter due to increased noise increases toward fainter magnitudes.

Because the cross-match between the SExtractor catalog and the lightcone catalog gives us the `GALAXYID` of each galaxy in the images, this provides us also with a direct link to all the available physical quantities in the semi-analytic snapshot catalogs, the dark matter halo catalogs, and the underlying dark matter density fields, such that it becomes possible to perform numerous experiments related to how well we can extract such physical parameters starting from any kind of observation that can be modeled using the MRObs.

3 EXAMPLE: SIMULATING CANDELS DATA

Large extra-galactic surveys often have complicated tiling patterns, exposure time variations, and masked regions across their total field of view that complicate the analysis. It can be convenient to include these kind of effects into the image simulation. This ensures that the signal-to-noise properties and the geometry of the real and mock data sets are comparable. Here we will illustrate the technique that we use to accomplish this by performing a mock image simulation of the ongoing multi-cycle treasury program Cosmic Assembly Near-Infrared Deep Extragalactic Legacy Survey (CANDELS; Grogin et al. 2011; Koekemoer et al. 2011, HST Programs 12060–

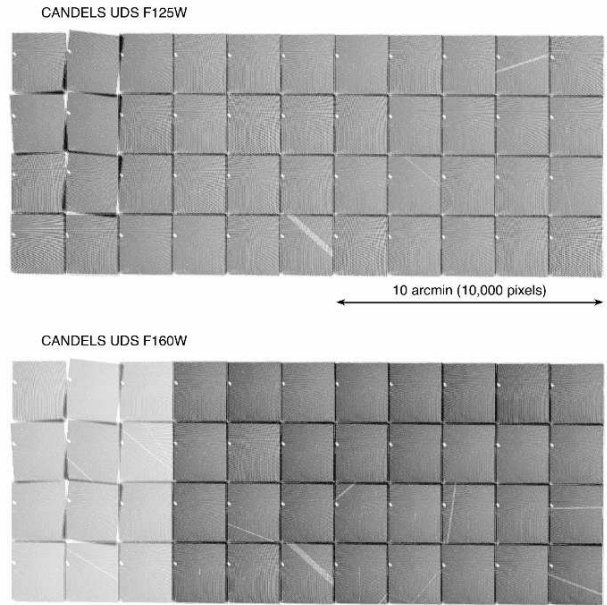


Figure 13. CANDELS UDS inverse variance weight maps. The total field of view measures $23' \times 10'$, and is constructed from 44 individual tiles observed with HST/WFC3 in the filters F125W and F160W.

12064, 12440; PI: S. M. Faber) that primarily observes with the WFC3 on HST.

3.1 The CANDELS observations

Part of the ongoing HST CANDELS program, the UKIDDS Deep Survey (UDS) field measures approximately $23' \times 10'$ in the filters F125W (J_{125}) and F160W (H_{160}). This field of view is covered with 44 individual pointings with HST/WFC3 resulting in the tiling pattern shown in Fig. 13. For each tile, four exposures were obtained in both filters, resulting in average total exposure times across the field of 1900 s in F125W and 3300 s in F160W. The data were combined onto a common output frame measuring about $22,000 \times 10,000$ pixels with a pixel scale of $0''.06$ using the MULTIDRIZZLE software (Koekemoer et al. 2003; Fruchter et al. 2009). The resulting PSF in the drizzled data measures $0''.12$ (F125W) and $0''.18$ (F160W) in FWHM (Fig. 14). How well can we simulate these kind of data based on cosmological simulations using the MRObs?

3.2 The CANDELS simulation

Using the procedures outlined in §2.6 we can produce highly accurate mock ‘CANDELS’ data in a number of complementary ways.

(1) The first and most cumbersome method would be to produce each individual CANDELS tile at the correct telescope position and roll angle, and then to process the entire data set through MULTIDRIZZLE analogous to the processing performed on the real data. While this is certainly possible, for many scientific applications a good match between the simulated and real data sets can already be obtained by side-stepping the laborious drizzling process.

(2) The simplest and most straightforward way is to directly generate mock images the size of the entire UDS field based on our

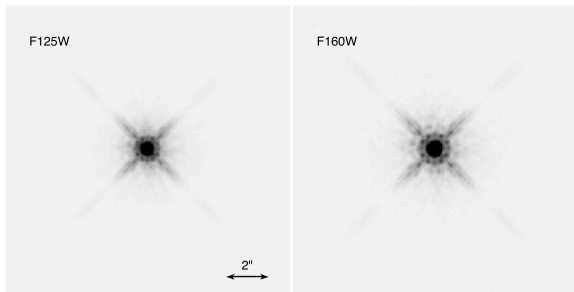


Figure 14. Images of the PSF in the filters F125W and F160W of the CANDELS UDS field. Our mock ‘perfect’ images are convolved with these PSFs.

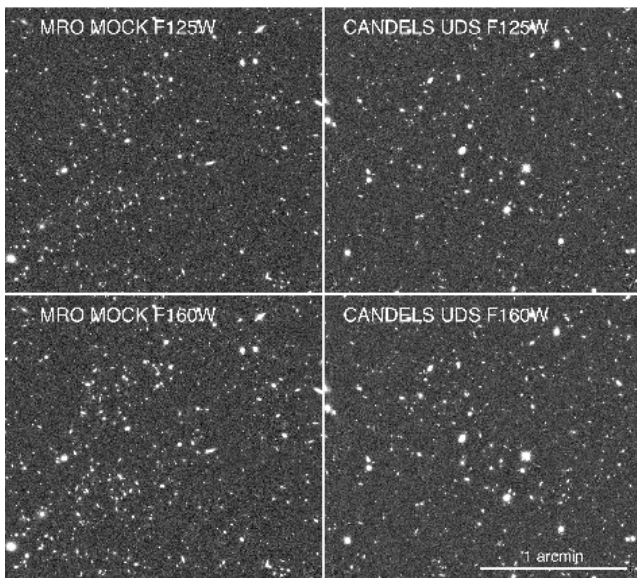


Figure 15. Simulated and real CANDELS UDS data in the filters F125W (top) and F160W (bottom). At a qualitative level the images appear already remarkably similar. Note that this is not only the result of our accurate image simulation technique, but also because our input galaxy population apparently has a striking resemblance compared with the observed one (e.g., in terms of number density, clustering, size and shape distributions, and brightness). Shown here is a region of about $2' \times 2'$ extracted from the wider $23' \times 10'$ UDS field.

model for the HST/WFC3 camera, the main UDS survey parameters, and a mock lightcone as input. This method produces mock UDS images for which the properties (e.g., noise, resolution) are, on average, very similar to those of the real survey. This is an extremely fast method for generating mock data sets that are approximately similar to the observations that are being modeled. It is also a powerful method to simulate images for a survey that has not (yet) been performed, or for simulating a survey at an arbitrary depth or field size.

(3) Our third method, the one that we will use for our demonstration, is an extremely powerful technique for generating a more precise simulation in which the pixel-to-pixel noise variations and geometry of the simulated images can be exactly matched to those of the real data. For this method we make use of ‘weight maps’ associated with the science data for many surveys. The CANDELS UDS weight maps (shown in Fig. 13) record the inverse variance of each pixel calculated during the image reduction pro-

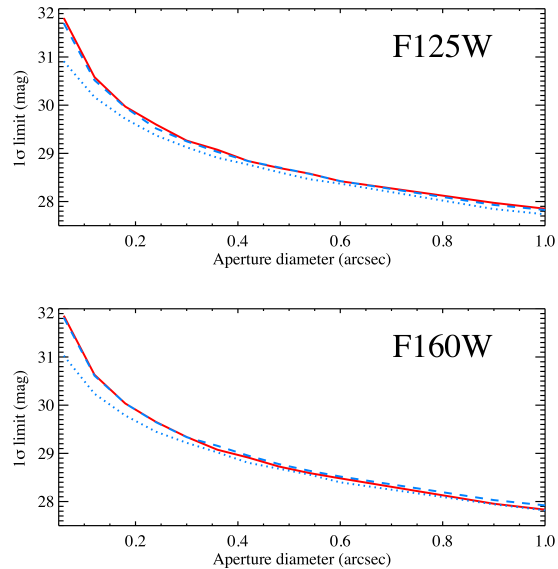


Figure 16. The background noise versus aperture size in the real CANDELS images (red solid lines) and our mock CANDELS images (blue dashed lines). The noise in the mock and real data is nearly identical. The true image noise in the absence of correlated noise introduced by the drizzling process is somewhat higher (blue dotted lines).

cess (Koekemoer et al. 2011). The HST inverse variance images (in units of $(e^-s^{-1})^{-2}$) are usually calculated as follows

$$\text{Inverse Variance} \approx \frac{(ft)^2}{(D + fB) + \sigma_{\text{ron}}^2}, \quad (6)$$

where f is the inverse flat-field, t is the exposure time, D is the accumulated dark current, B is the accumulated background, and σ_{ron} is the read-out noise (Koekemoer et al. 2011). The weight map includes all sources of instrumental and background noise, but not that of the science objects themselves to allow proper photometry with tools like SExtractor. As a first step we therefore produce simulated images that include the PSF-convolved objects (including the Poissonian object noise) but not the simulated background and read-noise we would normally apply. Instead, we add in these sources of noise by directly taking them from the inverse variance maps. As a final step we need to take into account that in the real CANDELS images the noise is spuriously correlated as a result of the drizzling process used to combine the many individual exposures. The amount of noise correlation depends on the multidrizzle parameters, which for the CANDELS UDS data amounts to a pixel rms noise reduction of a factor of 2 (Casertano et al. 2000). We introduce this noise correlation in our mock images by smoothing the mock images with a small Gaussian kernel (of about 1.5 pixels FWHM, in this case).

In the left panels of Fig. 15 we show a portion of the final simulated CANDELS images in the filters F125W and F160W. In the panels on the right, we show a region of the real CANDELS UDS images, displayed at the same zoom level and at the same colour stretch as the mock images shown on the left. At a qualitative level the images are remarkably similar. Note that this is not only the result of our accurate image simulation technique, but also because our input galaxy population apparently has a striking resemblance to the observed one (e.g., in terms of number density, clustering, size and shape distributions, and brightness). However, before we can compare the galaxy populations in the simulated and the real

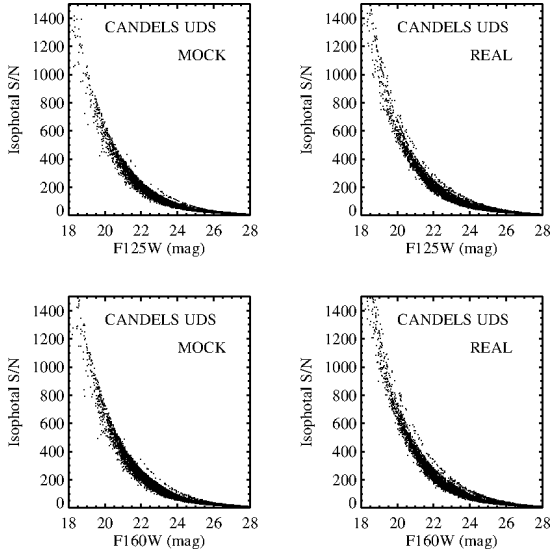


Figure 17. The isophotal signal-to-noise ratio in J_{125} and H_{160} versus the total magnitude of detected objects as measured by SExtractor. The signal-to-noise ratio distributions in the mock and the real CANDELS images are very similar.

data, we need to ensure that the image properties of our simulated data are indeed quantitatively similar to the real data. In Fig. 16 we show the measured background noise fluctuations as a function of aperture diameter as measured in the real CANDELS images (red solid lines) versus that measured in our simulated data set. The blue dotted lines indicate the (true) noise level in the absence of correlated noise. When we introduce the correlated noise resulting from the drizzling process, we get a near perfect match between the simulated (blue dashed lines) and real (red solid lines) CANDELS UDS images. As a second test, we look at the distribution of signal-to-noise (S/N) for objects detected in the real and simulated images. We ran SExtractor using identical detection parameters on the real and simulated images, and plot the isophotal S/N versus the measured magnitudes. The result is shown in Fig. 17 for the mock data (left panels) and the real data (right panels). Again, the S/N distributions are very similar between the real and simulated data, indicating that our image simulations are accurate.

In §4.1 we show an application of these CANDELS simulations by comparing the galaxy number counts in our semi-analytic mock lightcones with those extracted from our mock images, and with those in the real CANDELS images. The simulated CANDELS data produced here are part of our first scientific data release as announced in §5.

4 EXAMPLES OF APPLICATIONS

4.1 Galaxy number counts in CANDELS

One of the most basic tests that are used to test the accuracy of semi-analytic model predictions is to compare the number counts of galaxies observed as a function of apparent magnitude in some band with those predicted by a mock lightcone observation constructed from the semi-analytic model as described in §2.4. However, as discussed in the introduction, these light-cones do not suffer from any of the observational effects afflicting real observations.

The MRObs approach to modeling discussed in sections 2.5

to 2.7 allows us to make comparisons between observations and semi-analytic predictions in a highly realistic way. By simulating a mock survey matched to the real observations that one wants to compare with, and then running source extraction and photometry software on the mock and real images in identical manner, we can in principle assess how certain observational biases affect the interpretation of the real data, and how this impacts on our comparison of those real data with the simulations. Of course, one has to be aware that other biases may be introduced simply due to the fact that the models are likely no perfect match to the real data.

As a first example, we compare the number counts measured from a mock lightcone to those derived from our mock images based on that lightcone. Fig. 18 shows the two types of number counts from our simulated CANDELS UDS data in blue compared to the plain light cone data in black. The counts extracted from the simulated image were not corrected for completeness. At bright magnitudes ($J_{125}, H_{160} \lesssim 22$ mag) the counts are in good agreement, but they diverge toward fainter magnitudes counts detected in the images compared to the lightcone on which the mock images are based. The extracted counts are about a factor of 2 lower than the lightcone counts at $J_{125}, H_{160} \sim 26.5$ mag.

The red lines in the figure show number counts measured in the real CANDELS UDS data (no completeness corrections applied). At the faint end, the lightcone substantially over-predicts the observed counts, similar to discrepancies between semi-analytic predictions and observations found in earlier studies. However, it is very interesting to note that the difference between the semi-analytic predictions and the real number counts becomes smaller when we compare the real data to our mock data. Simply by ‘observing’ the lightcone we already lose a significant number of galaxies that would not be detected in a real observation (if the lightcone was an accurate reflection of reality).

The results presented in Fig. 18 suggest that it is important to take observational effects into account when comparing real data with simulations. These effects need to be quantified before one can change the parameters in a semi-analytic model to better match the observations. With the mock data produced by and published through the MRObs these tests can now be performed easily. A more detailed analysis of the number counts in synthetic observations as predicted by the MRObs compared to those predicted by ordinary semi-analytical models will be presented in a follow-up paper.

4.2 The properties of galaxy clusters at low and high redshift

Our new lightcone ‘aiming’ technique described in §2.4.2 offers an efficient way for predicting the detailed observational properties of, for example, galaxy clusters. Here we present mock SDSS and HST observations of a massive galaxy cluster at different redshifts and orientations. The cluster was selected from the roughly 3,000 clusters in the MR, and has a total dark matter mass of $\sim 7 \times 10^{14} M_{\odot}$ at $z = 0$. The selection was performed using the table of friends-of-friends groups in the MRDB. After finding FOF groups in the right mass range, a random selection was made of a cluster. That cluster was traced backwards in time using the table with halo merger trees. At desired redshifts the position of the cluster’s main progenitor was returned. That position, together with a direction and using the co-moving distance corresponding to the redshift, was used to define a light cone that had the cluster at its center and at exactly the correct redshift. This cone was then observed using a few different virtual telescope configurations.

In the first example, we have produced mock SDSS images in

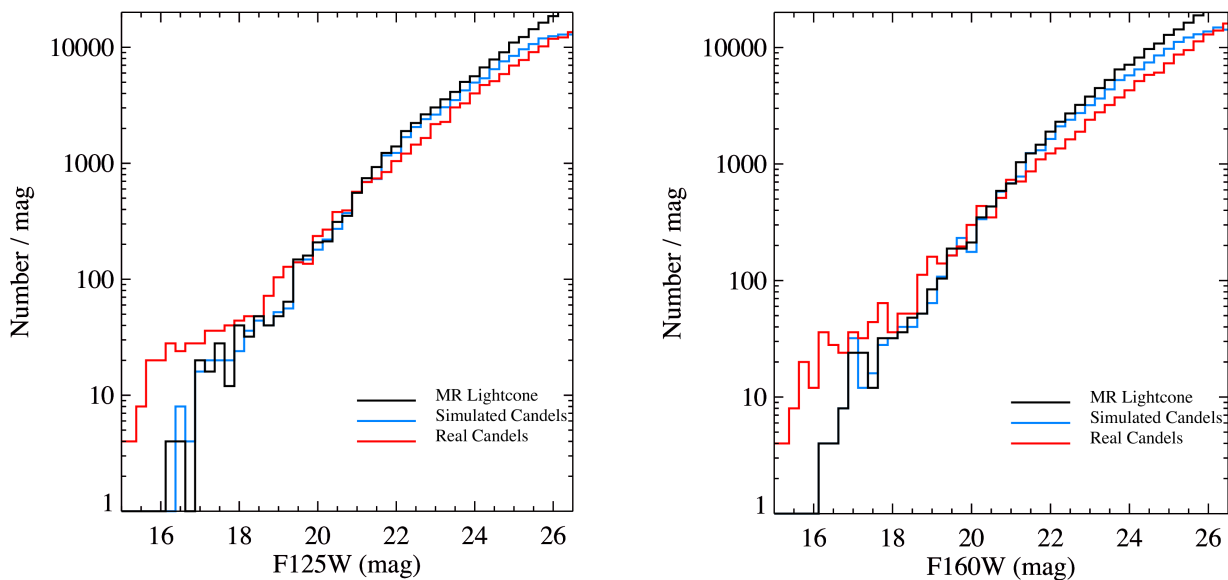


Figure 18. Galaxy number counts in J_{125} and H_{160} as a function of magnitude in the lightcone (black solid line), the real CANDELS UDS data (red solid line), and those extracted from the simulated CANDELS UDS data (blue solid line). While the lightcone data is known to over-predict the observed number counts to some extent, the discrepancy between the observations and the model predictions is significantly reduced after folding the lightcones through the MROBs and performing object detection and photometry from the mock images as performed on the real images. The large difference between the real and simulated data at the bright end is due to Galactic stars that are absent in our simulations.

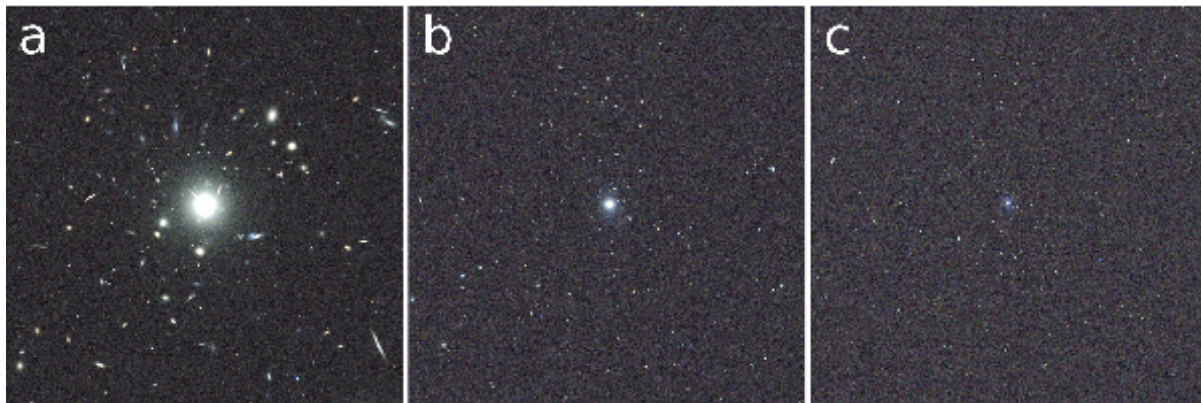


Figure 19. A high-mass galaxy cluster as it would appear at redshifts of $z \approx 0.02$ (panel a), $z \approx 0.09$ (panel b), and $z \approx 0.21$ (panel c) in an SDSS-type survey. These cluster images are based on our lightcone aiming technique described in §2.4.2.

$g'r'i'$ showing what this cluster would look like at redshifts from $z = 0.02$ to $z = 0.21$ (Fig. 19). These mock data can be compared directly with real clusters found in the SDSS. It is clear from Fig. 19 that the study of galaxy clusters in the SDSS survey becomes challenging already at moderately high redshifts. As a second example, we therefore show a mock image of the same cluster, now seen at $z = 0.4$ and observed with HST/ACS in the filters $g_{475}r_{625}z_{850}$ (Fig. 20, left panel). In the right panel we show an actual HST image of the well-studied $z = 0.4$ cluster Cl0024 with a comparable dark matter mass (Jee et al. 2007; Harsono & De Propris 2009). The images were produced using identical parameter settings in the software that produces the colour images from the `.fits` files (see §5.4.1). Although both clusters have a dominant population of red sequence galaxies that appear almost identical in these HST/ACS colours, the real cluster appears to have a greater number of cluster galaxies than the mock cluster. The MR contains thousands of

these type of galaxy clusters suitable for data-mining. Users will be able to use mock observations such as these to compare the properties of simulated and real clusters in a quantitative manner. Our third example highlights another unique feature of our improved lightcone technique, which allows us to produce observations of structures seen from different directions. Each light cone is created following the same principle as above, the only difference being that the cluster is observed from different directions. In Fig. 21 we show mock HST images in $V_{606}i_{775}z_{850}$ of the same cluster shown before, but now at $z \approx 1.07$. Panels show the exact same cluster viewed from three different directions, with (proto-)cluster galaxies having $\log M_* > 10M_\odot$ marked with white circles. The large yellow circle marks the virial radius of the central halo. While the projected distribution of cluster galaxies appears roughly spherical in the first two orientations (left and middle panels), it is much more filamentary in the third orientation (right panel). The line of sight

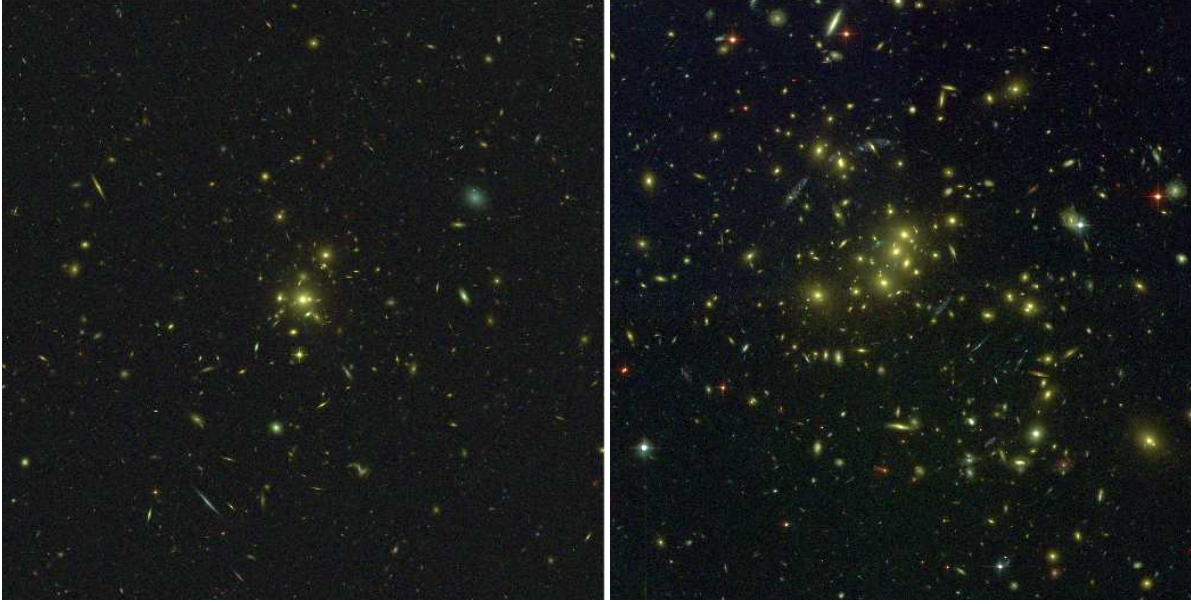


Figure 20. Mock HST/ACS $g_{475}r_{625}z_{850}$ image of a massive galaxy cluster in the MR simulations seen at $z = 0.4$ (left) versus a real HST/ACS $g_{475}r_{625}z_{850}$ image of the galaxy cluster Cl0024 at $z = 0.4$ (Jee et al. 2007) (right). These cluster images are based on our lightcone aiming technique described in §2.4.2.

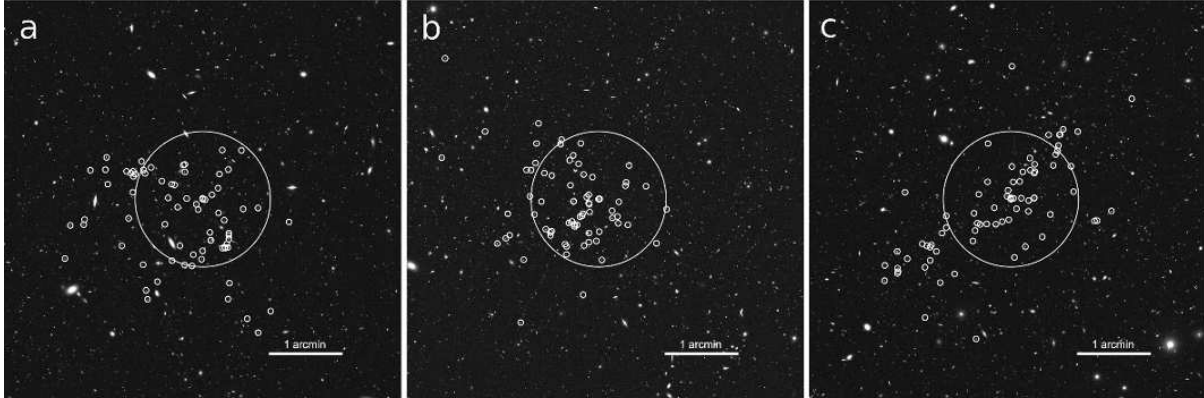


Figure 21. Mock HST/ACS $V_{606}i_{775}z_{850}$ colour composite image of a massive galaxy cluster at $z \approx 1.07$ viewed from three different directions. While the projected distribution of cluster galaxies appears spherical in the first two orientations (left and middle panels), it appears highly filamentary in the third orientation (right panel), indicating that projection effects can be important. The virial radius of the central halo is marked by a yellow circle.

velocity dispersions in the three cases are 807, 704, and 568 km s^{-1} . This example illustrates that projection effects are important to take into account when studying the assembly of galaxy clusters, especially at high redshift where both the samples of clusters and the number of identified cluster galaxies are relatively small. The multi-wavelength nature of the MRObs data allows for the detailed testing, calibrating and tuning cluster detection algorithms using physically-motivated cluster samples.

4.3 Colours and structural properties of galaxies

Another new test facilitated by the MRObs is comparison of the structural properties of galaxies in the semi-analytic model to those in real observations. In Fig. 22 we show a stellar mass versus SFR diagram for galaxies between $z = 1.5$ and $z = 2.5$ selected from one of our mock lightcone catalogs. In the panel on the right, we

show $1'' \times 1''$ postage stamps indicating the appearance of these galaxies in our simulated HST data (the image stamps are drawn from a mock $B_{435}, i_{775}, H_{160}$ colour-composite image based on the HST/ERS survey). These mock data can be used to measure galaxy structural properties (e.g., Sersic index, bulge-to-disk ratio, inclination), sizes and colours in exactly the same way as typically performed on real data only. By comparing measurements made based on the mock images with the exact physical quantities given by the semi-analytic model users could test how well such values can be recovered for a given data set, or for a given galaxy population. It also allows users to compare the structural properties of mock and real galaxies in a relatively unbiased way.

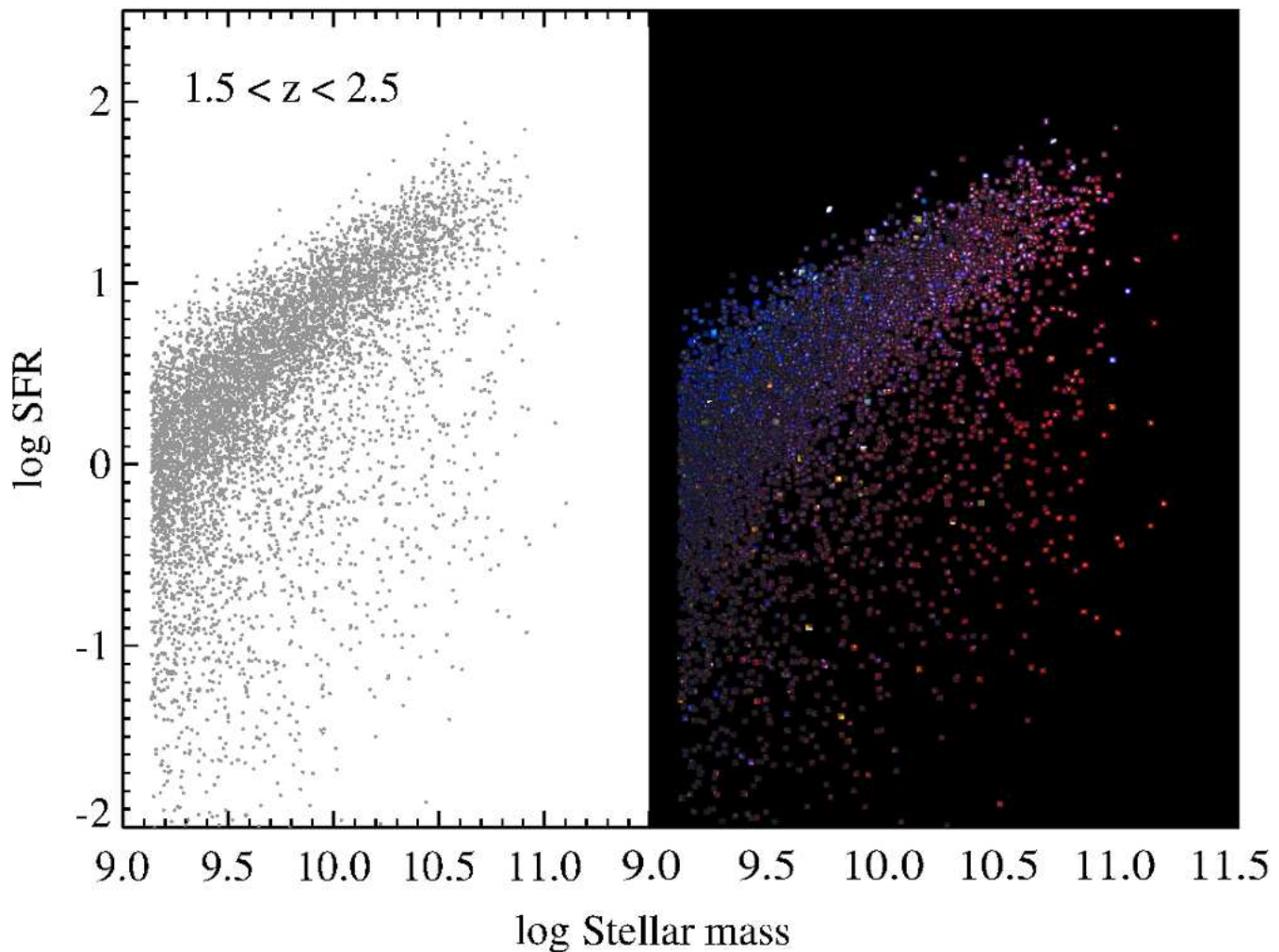


Figure 22. MRObs visualisation of the structural properties of galaxies as predicted by the semi-analytic model. In the left panel we show the stellar mass versus SFR diagram for galaxies between $z = 1.5$ and $z = 2.5$ made directly from the lightcone catalog. In the panel on the right, we show the actual morphologies of the galaxies as predicted by the SAM by showing $1'' \times 1''$ postage stamps extracted from a simulated HST image (the image stamps were taken from a mock $B_{435}, i_{775}, H_{160}$ colour-composite image based on the HST/ERS survey). Quiescent objects that lie below the main star-forming sequence appear both redder and more compact compared to objects on the star-formation sequence. The colours, sizes and structural properties of these type of galaxy images can be compared directly to those of galaxies found in real data.

4.4 Selection of high redshift dropout galaxies

The last example we show here is the use of the MRObs in the selection of high redshift dropout galaxies from deep multi-wavelength imaging surveys and predictions thereof (e.g. Baugh et al. 1998; Blaizot et al. 2004; Guo & White 2009; Overzier et al. 2009a). In Fig. 23 we show the colour-colour diagrams typically used to isolate galaxy samples at $z \sim 4$ (B_{435} -dropouts), $z \sim 5$ (V_{775} -dropouts), and $z \sim 6$ (i_{775} -dropouts). Objects at these high redshift suffer severe attenuation from the IGM in their spectra blue-ward of $\text{Ly}\alpha$ (see §2.5). Consequently, these objects can be isolated from lower redshift galaxy population, as their Lyman break redshifts through a strategically chosen set of filters. Panels on the top show colour distributions for all objects found in one of our mock lightcones. The bottom panels show those objects that were detected in a mock survey based on the same lightcone. The limiting magnitudes used for the lightcone and for the extracted catalog were the same. This figure highlights some of the main differences between a pure semi-analytic model

prediction (top panels) and what an observer actually sees (bottom panels). The colours of galaxies extracted from mock images are significantly scattered compared to their true (input) colours, making it harder to distinguish between low and high redshifts, or to derive their physical properties (e.g., redshift, mass, dust, star formation history, SFR) based on fitting their observed colours to a set of spectral synthesis models. It is straightforward to study and quantify such effects through the use of these kind of mock data. In the MRDB SQL queries can be performed to cross-match the SExtractor output catalogs to the lightcone or semi-analytic input catalogs, allowing one to investigate in detail the offsets between intrinsic and apparent properties, and to study which galaxies are included and excluded by certain observational selection criteria (e.g. colour-colour selections).

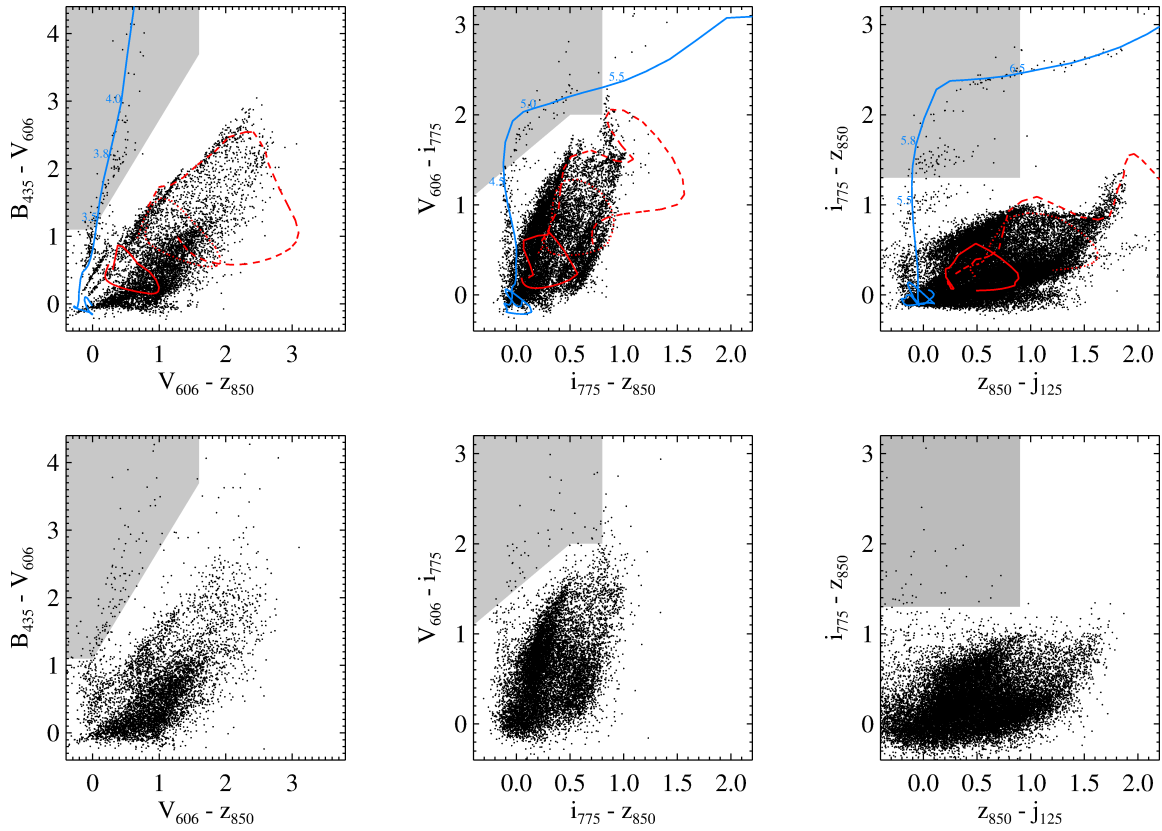


Figure 23. Colour-colour diagrams commonly used to select galaxy samples at $z \sim 4$ (B_{435} -dropouts, left panels), $z \sim 5$ (V_{606} -dropouts, middle panels), and $z \sim 6$ (i_{775} -dropouts, right panels). Panels on the top show the colour distributions of all objects in the lightcone. Panels on the bottom show the colour distribution of the objects detected in mock images based on the same lightcone. Tracks indicate the typical colours of simple galaxy templates for various low redshift populations (red lines; irregulars: solid, Sbc: dotted, Elliptical: dashed) and high redshift dropouts (blue, with redshifts marked along the tracks). Shaded regions mark the colour-colour selection windows commonly used to select high redshift dropout candidates.

5 PUBLIC ACCESS TO THE MROBS DATA

5.1 MRObs database

As described above, the MRObs builds upon and extends the popular MRDB. Apart from the images, all the datasets produced by the MRObs and described in this paper are stored in a database that is accessible through the same interface as the MRDB itself⁷ and can be directly joined to the existing data sets. Here we give a summary description of the database and access methods, focusing on the new data products and how they are linked to the existing ones.

The MRDB is a relational database⁸, where data sets are stored in tables (relations). A table generally stores objects of a particular type, with properties of these objects stored in columns. For example we have tables storing the the positions and velocities of particles from an N-body simulation, albeit a small one. We have tables with FOF groups and sub-halos as well as galaxies and many more. The web site giving access to these tables provides all information about the structure of the database.

An important feature of relational database design in general,

and the MRDB in particular, is the possibility to manifest relations or links between objects in different tables. For example, a galaxy in the Munich semi-analytical model is always embedded in a subhalo. This relation is stored in the tables with galaxies as a column storing the (unique) identifier of the corresponding halo. The MRDB has a particularly rich set of such relations, especially where it deals with the relations between objects of the same type at different times (Lemson & Virgo Consortium 2006).

Recent additions to the database were the results of the latest version of the Munich SAM from Guo et al. (2011) and pencil-beam and all sky light-cones derived from these in Henriques et al. (2012). The images produced by the MRObs from such light-cones do not lend themselves easily for storing in a database. However the SExtractor catalogues extracted from the images have been stored and we also have tables storing the different IGM absorption models described in §2.5. More information and examples on how to apply and cross-correlate the various MRDB and MRObs data sets are documented at the URL given below.

5.2 Data products of the MRObs

The MRObs delivers a number of entirely new data products to the community that are useful for independent analysis, or for serving as the starting point for new simulations. Here we will briefly describe the different types of new products.

⁷ See <http://gavo.mpa-garching.mpg.de/Millennium> for a publicly accessible website giving access to the milli-Millennium database and information on how to gain access to the full database.

⁸ This is not the place to describe relational databases in detail, there is sufficient information available online.

5.2.1 Multi-wavelength lightcone catalogs with structural properties

The random field lightcones released as part of this paper are identical to the 24 multiwavelength lightcones measuring $1.4^\circ \times 1.4^\circ$ on the sky from Henriques et al. (2012), but with structural information added. The new structural information (sizes of the disk and bulge components, inclinations and position angles) is crucial for building the accurate galaxy models predicted by the MR simulations. These lightcones can be used, for example, to compare structural properties measured off the simulated images to the true input values. They can also be used as the starting point for users wishing to perform their own image simulations using realistic input catalogs based on the MR. In addition to the ‘random’ lightcones, we also release entirely new lightcones that specifically target galaxy clusters at a range of redshifts (see §2.4.2 and §4.2). All these lightcone catalogs are made available through the MRDB.

5.2.2 IGM tables

We provide tables that list the mean IGM attenuation as a function of redshift for a range of models (see §A). The IGM tables are applied to the lightcones to predict accurate colours and magnitudes of galaxies with redshift.

5.2.3 Object lists

Information from the structural light cones, the IGM tables, and a plate scale are combined to generate the input to the SkyMaker code that we use to create our synthetic ‘pre-observation’ images. These object lists may be used by other synthetic image simulators.

5.2.4 Pre-observation maps (‘perfect’ model images)

As described in §2.6, for each filter we build a so-called pre-observation or ‘perfect’ image that is based on the input object list. These images can be seen as a representation of the sky free of noise, PSF, or background. As such, they are easily convolved, rebinned, and scaled to match an arbitrary observation (typically a combination of a given telescope, camera, and exposure).

5.2.5 Simulated images

The ‘perfect’ images are turned into synthetic images that simulate real observational data. These images can be downloaded for further analysis. We also provide the PSF images that were used to convolve the perfect images to the instrument resolution, as well as documentation providing full details of how the images were produced.

5.2.6 SExtractor products

The simulated images are processed using SExtractor to produce the so-called segmentation maps identifying which image pixels correspond to which detected object, as well as the standard SExtractor output photometry catalogs. The SExtractor catalogs are made available through the MRDB where they can be searched or cross-matched with other data, such as lightcone catalogs, semi-analytic snapshots, dark matter halos, or density fields. The segmentation images are available for download.

5.3 Simulated surveys currently available in the MRObs

In its current deployment, the MRObs offers a number of data sets conveniently matched to some of the most popular extra-galactic surveys (e.g. the SDSS, CFHT-LS Wide and Deep, GOODS, UDF, GOODS/ERS, and CANDELS) for use by the community. Updates and future data releases will be announced through the MR web portal (URL given below), and in forthcoming publications.

5.4 The MRObs image browser

A special feature of the MRObs is that many of the data sets can also be accessed directly by means of our interactive MRObs image browser. This is an online tool that allows users to scan over and zoom into the synthetic images. These images are linked to the backend database (the MRDB) through a simple point-and-click function that allows retrieval of detailed information about the galaxies that are displayed. This is useful, for example, for familiarizing oneself with the relation between physical and observed properties of different types of galaxies or galaxies at different redshifts, for selecting interesting objects from the MR simulations for subsequent analysis, for comparing the quality expected for different types of data sets or telescopes, and for didactical and outreach purposes. Here we describe the main features of the MRObs browser in brief.

5.4.1 Deep zoom RGB image pyramids

The images produced by the MRObs are typically very large. For example, a simulated HST survey covering an area of $30' \times 30'$ at a (drizzled) pixel scale of $0''.09$ already measures $20,000 \times 20,000$ pixels (400 Megapixels), and in principle the MRObs could create much larger fields at much higher resolution than this. These images therefore do not fit on a standard computer screen. Using a technology similar to, e.g., Google Maps, the MRObs browser allows users to efficiently pan around and zoom in such large, high resolution images. We here describe in some detail how we have implemented this truly virtual telescope.

First the simulated, multi-wavelength filter images are combined into false-colour RGB composites. We use the publicly available code STIFF⁹ that handles the conversion from arbitrarily large scientific FITS input images to standard TIFF format output images (Bertin 2012). STIFF automatically (or manually) applies contrast and brightness adjustments, colour balance and saturation, and gamma corrections producing colour images that are highly informative of the level of detail present in the mono-chromatic input fits images. When we have multiple bands available for any of the three RGB channels (for example when making colour composites of data sets based on more than three filters), we reduce the number of input images to three by creating variance-weighted averages and use those as the input for each channel.

From this high-resolution image we then create a so-called ‘image pyramid’ consisting of representations of this high resolution image at ever decreasing resolution. The method is illustrated in Fig. 24. The top of the pyramid (level 0) consists of a single $s \times s$ pixels low resolution image that is a heavily rebinned version of the original or full-resolution $N \times N$ pixels image. The next level contains $p^1 \times p^1$ image tiles each of p times higher resolution compared to the previous level. At the n th level (corresponding to

⁹ <http://astromatic.net/software/stiff>

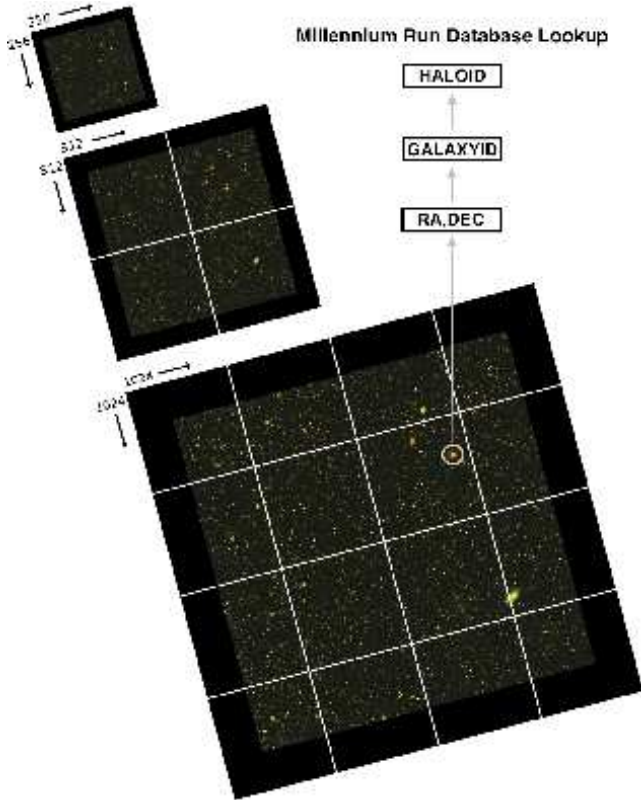


Figure 24. An image pyramid consisting of three levels is shown. At its lowest resolution level, the image consists of a single 256×256 pixels tile having 1/4th of the true image resolution. At the base of the pyramid, the image is divided into 4×4 full-resolution tiles each measuring 256×256 pixels. The MRObs deep zoom image browser makes heavy use of these kinds of tilings for an efficient viewing of the data. The browser also makes a translation between pixel coordinates and WCS coordinates within each viewport. This conveniently enables the user to retrieve high-level properties of any object found within the image by matching its sky coordinates to the underlying lightcone catalog, and by querying the galaxy or halo catalogs stored on the MRDB server based on the `GALAXYID` or `HALOID` of any matches found.

the base of the pyramid), there will be $p^n \times p^n$ tiles each representing only a small portion of the original image but now at its highest resolution.

The browser software¹⁰ uses this data format to download only those tiles that at the current zoom level are required to show the image. This significantly reduces the download time and creates a smooth transition between the different levels or different regions of the image when viewed in a web browser. For example, if we adopt a factor of $p = 2$ scalings between levels, tiles of $s = 256$ pixels, and an original image of $N = 32,768$ pixels, the last level (level 7) will consist of 128×128 tiles of 256×256 pixels. This means that only about 0.1% of data needs to be downloaded at any time to display a particular region at its fullest resolution on a 1024×1280 resolution display.

¹⁰ We use the Deep Zoom technology developed by Seadragon/Microsoft embedded in custom written java script libraries.

5.4.2 User interface of the MRObs browser

The MRObs Browser offers the user the choice of a large number of image pyramids, based on sets of different mock images, for a variety of virtual telescopes and with different wavelength bands. Each mock image is derived from a light cone stored in the MRDB, and the MRObs Browser allows interactive querying of these cones.

Screen-shots of an HST simulation viewed through the MRObs Browser are shown in Fig. 25. Clicking the image leads to an SQL query being submitted to the database that searches for the nearest galaxy to the selected (virtual) sky position, up to a maximum radius (currently $1''$). If a galaxy is found a large amount of information is retrieved and displayed in a table on the screen next to the image, as shown on the right hand side of the screenshots in Fig. 25. The selected galaxy is indicated on the image with a little white square (top panel). The table includes information of the galaxy on the light cone, such as redshift, apparent sizes and luminosities in up to 40 bands. The observed-frame SED is shown in graphical form above the table. It also includes, through the linking of the light-cone galaxy to the underlying semi-analytical galaxy catalogues, information about physical parameters such as stellar mass, gas mass, metallicities and rest frame magnitudes in the SDSS bands. The information also includes details about the original dark-matter subhalo and friends-of-friends group the galaxy belongs to. The latter information can in its turn be used to search for all other galaxies in the image that belong to the same FOF group as the selected galaxy. In the bottom panel, the positions of all galaxies that were retrieved are indicated on the screen. The structure turns out to be a galaxy group at $z \approx 0.5$.

The query capabilities of the MRObs Browser will be extended over time and will be tied to the plain SQL query capabilities of the MRDB.

6 FUTURE DEVELOPMENTS

Future refinements of the modeling recipes in the MRObs currently in preparation include the calculation of extinctions based on the physically motivated inclinations of galaxies (§2.4.3), as well as the inclusion of strong gravitational lensing based on the distribution of dark matter halos along each lightcone. Although the current simulations span the observed far-UV to the observed near-IR, improvements in the dust-modeling should eventually allow us to construct images out to far-infrared and sub-mm wavelengths. Future simulated surveys will be made available through the MRObs web portal. Ultimately, fully interactive, online versions of the SAM, the lightcone generator, and the telescope simulator will allow users of the MRObs even greater flexibility in performing the simulations that best suit their needs.

7 SUMMARY

In order to make predictions in the observational plane and to allow unbiased comparisons between semi-analytic models and real data, we have developed the Millennium Run Observatory (MRObs), a new virtual telescope facility that can be used to simulate realistic observational data based on the semi-analytic model galaxy catalogues associated with the dark matter MR simulations. The MRObs allows one to produce *scientific* image data sets in `.fits` format. These artificial data can be analyzed using the standard tools routinely used for analyzing real observations, allowing a relatively unbiased comparison between SAMs and real data. This

- Provide a framework for future virtual theoretical observatories

One of the great advantages provided by our extended modeling approach is that for the synthetic observations produced by the MRObs, the physical properties (e.g., dark matter halo mass, SFR, stellar mass, size, redshift) and photometric properties (e.g., magnitudes and colours) of every galaxy are precisely known, in contrast to real observations where one does not know the exact or ‘true’ answer. This makes the MRObs an ideal facility for calibrating many of the measurement and analysis techniques that are applied to real observations. The MRObs will allow observers and theorists to approach a problem from different directions with freedom in deciding where to meet.

We have introduced a modified lightcone technique that allows us to create lightcones aimed at selected objects or regions placed at any desired position or orientation. The new technique is useful for extending the range of questions that can be asked of the MRObs, such as what would be the appearance of a particular galaxy cluster at $z \sim 1$? What does this same cluster look like at $z \sim 6$ or at $z = 0$? How is the interpretation of observations of such structures affected by viewing angle or chance superpositions? Special cones centred on clusters at a range of redshifts have been added to the MRDB for studies of cluster evolution.

Attenuation by the IGM is applied to the lightcones statistically using the baseline model from Madau (1995), as well as two more recent implementations based on Monte Carlo modeling of the IGM by Harrison et al. (2011). Our IGM attenuation tables have also been added to the MRDB such that they can be used to apply ‘on the fly’ IGM absorption corrections to lightcones (see the MRObs URL for a tutorial on how to apply the IGM absorption corrections to the lightcones from Henriques et al. (2012) also available in the MRDB). This is essential for making comparisons with high redshift observations.

In order to allow the community to use our predictions as the basis for other mock observation experiments, we provide not only our final image products, but also the intermediate steps such as the input object lists and the pre-observation model images.

In order to introduce the communities of theoretically and observationally inclined researchers to the ‘added value’ of the MRObs modeling approach, we have provided the following four example user cases:

(1) We compared the galaxy number counts in the CANDELS/UDS survey with the predicted counts taken directly from the semi-analytic lightcone and with the counts extracted from synthetic CANDELS images (Fig. 18 and §4.1). Interestingly, the counts recovered from the synthetic images are lower than those predicted by the lightcone that was used to construct the synthetic observation, suggesting that the discrepancy between semi-analytic model predictions and observations may be smaller than previously claimed. The implications of this will be detailed in a followup paper (Overzier et al., in prep.).

(2) We simulated images of galaxy clusters seen with SDSS and HST at a range of redshifts (Figs. 19–21 and §4.2). We also showed synthetic images of the same galaxy cluster at $z = 1.1$ from three different directions, illustrating that orientation effects can be important when interpreting the visual appearance of large-scale structure at high redshift.

(3) We showed how the MRObs allows one to study the detailed structural properties of semi-analytic galaxies in synthetic images (Fig. 22 and §4.3). In these synthetic images one can measure colours, sizes, bulge-to-disk ratios and profile shapes using standard observational techniques. The outcome of these measurements can then be compared to the intrinsic values provided by the MRObs, or to measurements performed on real galaxies.

(4) We showed how the MRObs images can be used to search for high redshift dropout galaxies in a manner that is directly analogous to that used for real high redshift dropout searches (Fig. 23 and §4.4). This enables a much more realistic comparison with the data, and allows us to assess how well we are able to derive the intrinsic physical properties from the observations.

Extending the successful open-access approach of the MR project, we make available new data products for use by the community. As part of our first data release, we have produced simulated data that emulates a number of key surveys, including SDSS, CFHT-LS (Wide and Deep), GOODS, HUDF, GOODS/ERS, and CANDELS (UDS, COSMOS and GOODS-S). The data sets are modeled using two different cosmologies (WMAP1 and WMAP7), two spectral synthesis models (BC03 and M05), and three IGM absorption models (MADAU, MEIKSIN, and INOUE-IWATA). In specific cases, we provide synthetic images that have the exact same geometric and identical noise properties as the reference survey. The MRObs data can furthermore be explored using an online image browser that allows users to interactively explore the available mock observations. The browser graphically links objects (galaxies) in the synthetic images to various types of information available in catalogs in the MRDB. For each synthetic galaxy, this information includes the physical properties of their dark matter halos, the intrinsic properties of the galaxy itself, the absolute and apparent photometric properties, and the observed properties recovered from the synthetic images using SExtractor.

The public data and the MRObs browser can be accessed at the following URL:

<http://galformod.mpa-garching.mpg.de/mrobs/>

In conclusion, the MRObs allows us to study our simulated universes through the eyes of our telescopes. We hope that the methods and data presented in this paper will encourage others to take advantage of the new opportunities offered by this approach.

ACKNOWLEDGMENTS

We thank Rychard Bouwens, Yi-Kuan Chiang, Marijn Franx, Guinevere Kauffmann, Jaewon Kim, Ben Metcalfe, and Masami Ouchi for helpful discussions. We thank Chris Harrison for making his code IGMTransmission publicly available and for his clarifications. We thank Russell Ryan, Seth Cohen, Rogier Windhorst and other members of the GOODS ERS team for discussions and supplying us with their empirical PSFs. We thank Daniel Harsono for providing the HST/ACS images of Cl0024 used in Fig. 20. We thank Matthias Egger for his excellent technical support. The Millennium Simulation databases used in this paper and the web application providing online access to them were constructed as part of the activities of the German Astrophysical Virtual Observatory. This work was supported by Advanced Grant 246797 ‘GALFORMOD’ from the European Research Council. The authors acknowledge the

Table 1. List of filters currently available in the MRObs and the FILTERID under which they are known in the MR database.

FILTERID	Description	FILTERID	Description
U	Johnson <i>U</i>	ACS435	HST/ACS-WFC F435W
B	Johnson <i>B</i>	ACS475	HST/ACS-WFC F475W
V	Johnson <i>V</i>	ACS606	HST/ACS-WFC F606W
Rc	Cousins <i>R</i>	ACS625	HST/ACS-WFC F625W
Ic	Cousins <i>I</i>	ACS775	HST/ACS-WFC F775W
Z	UKIDDS <i>Z</i>	ACS814	HST/ACS-WFC F814W
Y	UKIDDS <i>Y</i>	ACS850	HST/ACS-WFC F850LP
J	UKIDDS <i>J</i>	GFUV	GALEX FUV
H	UKIDDS <i>H</i>	GNUV	GALEX NUV
K	Johnson <i>K</i>	NIC110	HST/NICMOS F110W
Ks	UKIDDS <i>K_s</i>	NIC160	HST/NICMOS F160W
i1	Spitzer/IRAC channel 1	VIMOSU	VLT/VIMOS <i>U</i>
i2	Spitzer/IRAC channel 2	WFC105	HST/WFC3-IR F105W
i3	Spitzer/IRAC channel 3	WFC125	HST/WFC3-IR F125W
i4	Spitzer/IRAC channel 4	WFC160	HST/WFC3-IR F160W
SDSS _u	SDSS <i>u'</i>	WFC225	HST/WFC3-UVIS F225W
SDSS _g	SDSS <i>g'</i>	WFC275	HST/WFC3-UVIS F275W
SDSS _r	SDSS <i>r'</i>	WFC336	HST/WFC3-UVIS F336W
SDSS _i	SDSS <i>i'</i>	WFPC300	HST/WFPC2 F300W
SDSS _z	SDSS <i>z'</i>	WFPC450	HST/WFPC2 F450W

Texas Advanced Computing Center (TACC) at The University of Texas at Austin for providing the 307 Mpixel tiled-display system (Stallion) and the 12.4 Mpixel multi-touch display (Lasso) visualization resources that have contributed to developing the methods and results reported within this paper. We thank Ben Urlick and Brandt Westing of TACC for their time and expert support.

REFERENCES

- Angulo, R. E., & White, S. D. M. 2010, *MNRAS*, 405, 143
- Angulo, R. E., Springel, V., White, S. D. M., et al. 2012, arXiv:1203.3216
- Baugh, C. M., Cole, S., Frenk, C. S., & Lacey, C. G. 1998, *ApJ*, 498, 504
- Baugh, C. M., Lacey, C. G., Frenk, C. S., et al. 2005, *MNRAS*, 356, 1191
- Benson, A. J., Bower, R. G., Frenk, C. S., et al. 2003, *ApJ*, 599, 38
- Bertin, E., & Arnouts, S. 1996, *A&AS*, 117, 393
- Bertin, E. 2009, *Memorie della Società Astronomica Italiana*, 80, 422
- Bertin, E. 2012, in *Proceedings of ADASS XXI* P.Ballester and D.Egret editors, in press
- Bertone, S., DeLucia, G., & Thomas, P. A., 2007, *MNRAS*, 379, 1143
- Bershady, M. A., Charlton, J. C., & Geoffroy, J. M. 1999, *ApJ*, 518, 103
- Blaizot, J., Guiderdoni, B., Devriendt, J. E. G., et al. 2004, *MNRAS*, 352, 571
- Blaizot, J., Wadadekar, Y., Guiderdoni, B., et al. 2005, *MNRAS*, 360, 159
- Bouché, N., Dekel, A., Genzel, R., et al. 2010, *ApJ*, 718, 1001
- Bouwens, R., Cayón, L., & Silk, J. 1999, *ApJ*, 516, 77
- Bouwens, R. J., Illingworth, G. D., Rosati, P., et al. 2003, *ApJ*, 595, 589
- Bouwens, R. J., Illingworth, G. D., & Magee, D. K. 2006, *Astronomical Data Analysis Software and Systems XV*, 351, 145
- Bower, R. G., Benson, A. J., Malbon, R., et al. 2006, *MNRAS*, 370, 645
- Boylan-Kolchin, M., Springel, V., White, S. D. M., Jenkins, A., & Lemson, G. 2009, *MNRAS*, 398, 1150
- Bruzual, G., & Charlot, S. 2003, *MNRAS*, 344, 1000
- Bruzual, G. 2007, *From Stars to Galaxies: Building the Pieces to Build Up the Universe*, 374, 303
- Cardelli, J. A., Clayton, G. C., & Mathis, J. S. 1989, *ApJ*, 345, 245
- Carlson, J., & White, M. 2010, *ApJS*, 190, 311
- Casertano, S., de Mello, D., Dickinson, M., et al. 2000, *AJ*, 120, 2747
- Cattaneo, A., Blaizot, J., Devriendt, J., & Guiderdoni, B. 2005, *MNRAS*, 364, 407
- Cattaneo, A., Dekel, A., Devriendt, J., Guiderdoni, B., & Blaizot, J. 2006, *MNRAS*, 370, 1651
- Ceverino, D., Dekel, A., & Bournaud, F. 2010, *MNRAS*, 404, 2151
- Chilingarian, I. V., Di Matteo, P., Combes, F., Melchior, A.-L., & Semelin, B. 2010, *A&A*, 518, A61
- Cirasuolo, M., McLure, R. J., Dunlop, J. S., et al. 2010, *MNRAS*, 401, 1166
- Cole, S., Aragon-Salamanca, A., Frenk, C. S., Navarro, J. F., & Zepf, S. E. 1994, *MNRAS*, 271, 781
- Cole, S., Hatton, S., Weinberg, D. H., & Frenk, C. S. 1998, *MNRAS*, 300, 945
- Cole, S., Lacey, C. G., Baugh, C. M., & Frenk, C. S., 2000, *MNRAS*, 319, 168
- Connolly, A. J., Peterson, J., Jernigan, J. G., et al. 2010, *SPIE*, 7738,
- Conroy, C., Gunn, J. E., & White, M. 2009, *ApJ*, 699, 486
- Croton, D. J., Springel, V., White, S. D. M., et al. 2006, *MNRAS*, 365, 11
- Cucciati, O., De Lucia, G., Zucca, E., et al. 2012, arXiv:1205.1517
- De Lucia, G., & Blaizot, J. 2007, *MNRAS*, 375, 2
- Davis, M., Huchra, J., Latham, D. W., & Tonry, J. 1982, *ApJ*, 253, 423
- Davis, M., Efstathiou, G., Frenk, C. S., & White, S. D. M. 1985, *ApJ*, 292, 371
- Dekel, A., Sari, R., & Ceverino, D. 2009, *ApJ*, 703, 785
- Diaferio, A., Kauffmann, G., Colberg, J. M., & White, S. D. M. 1999, *MNRAS*, 307, 537
- Dobke, B. M., Johnston, D. E., Massey, R., et al. 2010, *PASP*, 122, 947
- Dutton, A. A., van den Bosch, F. C., & Dekel, A. 2010, *MNRAS*, 405, 1690
- Eminian, C., Kauffmann, G., Charlot, S., et al. 2008, *MNRAS*, 384, 930
- Erben, T., Van Waerbeke, L., Bertin, E., Mellier, Y., & Schneider, P. 2001, *A&A*, 366, 717
- Finkelstein, S. L., Papovich, C., Giavalisco, M., et al. 2010, *ApJ*, 719, 1250
- Finlator, K., Oppenheimer, B. D., & Davé, R. 2011, *MNRAS*, 410, 1703
- Fioc, M., & Rocca-Volmerange, B. 1997, *A&A*, 326, 950
- Forero-Romero, J. E., Blaizot, J., Devriendt, J., van Waerbeke, L., & Guiderdoni, B. 2007, *MNRAS*, 379, 1507
- Fruchter, A., Sosey, M., et al. 2009, ‘The MultiDrizzle Handbook’, version 3.0, (Baltimore, STScI)
- Gibson, R. R., Ahmad, Z., Bankert, J., et al. 2011, *Astronomical Data Analysis Software and Systems XX*, 442, 329
- Girardi, L., Groenewegen, M. A. T., Hatziminaoglou, E., & da Costa, L. 2005, *A&A*, 436, 895
- González, V., Labbé, I., Bouwens, R. J., et al. 2011, *ApJL*, 735,

- L34
- Grogin, N. A., Kocevski, D. D., Faber, S. M., et al. 2011, *ApJS*, 197, 35
- Guo, Q., & White, S. D. M. 2009, *MNRAS*, 396, 39
- Guo, Q., White, S., Boylan-Kolchin, M., et al. 2011, *MNRAS*, 413, 101
- Guo, Q., White, S., Angulo, R. E., et al. 2012, *MNRAS*, submitted (arXiv:1206.0052)
- Hamana, T., Colombi, S., & Suto, Y. 2001, *A&A*, 367, 18
- Harrison, C. M., Meiksin, A., & Stock, D. 2011, arXiv:1105.6208
- Harsono, D., & De Propriis, R. 2009, *AJ*, 137, 3091
- Hatton, S., Devriendt, J. E. G., Ninin, S., et al. 2003, *MNRAS*, 343, 75
- Henriques, B., Maraston, C., Monaco, P., et al. 2011, *MNRAS*, 415, 3571
- Henriques, B. M. B., White, S. D. M., Lemson, G., et al. 2012, *MNRAS*, 421, 2904
- Heymans, C., Van Waerbeke, L., Bacon, D., et al. 2006, *MNRAS*, 368, 1323
- Inoue, A. K., & Iwata, I. 2008, *MNRAS*, 387, 1681
- Jee, M. J., Ford, H. C., Illingworth, G. D., et al. 2007, *ApJ*, 661, 728
- Jenkins, A., Frenk, C. S., Pearce, F. R., et al. 1998, *ApJ*, 499, 20
- Jonsson, P., Groves, B. A., & Cox, T. J. 2010, *MNRAS*, 403, 17
- Jonsson, P., Cox, T. J., Primack, J. R., & Somerville, R. S. 2006, *ApJ*, 637, 255
- Kang, X., Jing, Y. P., Mo, H. J., & Börner, G., 2005, *ApJ*, 631, 21
- Kauffmann, G., & White, S. D. M. 1993, *MNRAS*, 261, 921
- Kauffmann, G., White, S. D. M., & Guiderdoni, B. 1993, *MNRAS*, 264, 201
- Kauffmann, G., Colberg, J. M., Diaferio, A., & White, S. D. M. 1999, *MNRAS*, 303, 188
- Kauffmann, G., & Haehnelt, M. 2000, *MNRAS*, 311, 576
- Kereš, D., Katz, N., Fardal, M., Davé, R., & Weinberg, D. H. 2009, *MNRAS*, 395, 160
- Kitzbichler, M. G., & White, S. D. M. 2006, *MNRAS*, 366, 858
- Kitzbichler, M. G., & White, S. D. M. 2007, *MNRAS*, 376, 2
- Klypin, A. A., Trujillo-Gomez, S., & Primack, J. 2011, *ApJ*, 740, 102
- Koekemoer, A. M., Fruchter, A. S., Hook, R. N., & Hack, W. 2003, *The 2002 HST Calibration Workshop : Hubble after the Installation of the ACS and the NICMOS Cooling System*, Proceedings of a Workshop held at the Space Telescope Science Institute, Baltimore, Maryland, October 17 and 18, 2002. Edited by Santiago Arribas, Anton Koekemoer, and Brad Whitmore. Baltimore, MD: Space Telescope Science Institute, 2003., p.337, 337
- Koekemoer, A. M., Faber, S. M., Ferguson, H. C., et al. 2011, *ApJS*, 197, 36
- Kriek, M., van Dokkum, P. G., Franx, M., et al. 2006, *ApJL*, 649, L71
- Kriek, M., Labbé, I., Conroy, C., et al. 2010, *ApJL*, 722, L64
- Lacey, C. & Cole, S. 1994, *MNRAS*, 271, 676
- Lee, S.-K., Ferguson, H. C., Somerville, R. S., Wiklund, T., & Gialalisco, M. 2010, *ApJ*, 725, 1644
- Leitherer, C., & Heckman, T. M. 1995, *ApJS*, 96, 9
- Lemson, G., & Virgo Consortium, 2006, arXiv:astro-ph/0608019
- Lotz, J. M., Jonsson, P., Cox, T. J., & Primack, J. R. 2008, *MNRAS*, 391, 1137
- Lotz, J. M., Jonsson, P., Cox, T. J., & Primack, J. R. 2010, *MNRAS*, 404, 575
- Madau, P. 1995, *ApJ*, 441, 18
- Maraston, C. 1998, *MNRAS*, 300, 872
- Maraston, C. 2005, *MNRAS*, 362, 799
- Maraston, C., Daddi, E., Renzini, A., et al. 2006, *ApJ*, 652, 85
- Maraston, C., Pforr, J., Renzini, A., et al. 2010, *MNRAS*, 407, 830
- Marchesini, D., Whitaker, K. E., Brammer, G., et al. 2010, *ApJ*, 725, 1277
- Marinoni, C., Le Fèvre, O., Meneux, B., et al. 2005, *A&A*, 442, 801
- Meiksin, A. 2006, *MNRAS*, 365, 807
- Mo, H. J., & White, S. D. M. 1996, *MNRAS*, 282, 347
- Monaco, P., Fontanot, F., & Taffoni, G. 2007, *MNRAS*, 375, 1189
- Neistein, E., & Dekel, A. 2008, *MNRAS*, 383, 615
- Neistein, E., & Weinmann, S. M. 2010, *MNRAS*, 405, 2717
- Ouchi, M., Hamana, T., Shimasaku, K., et al. 2005, *ApJL*, 635, L117
- Overzier, R. A., Bouwens, R. J., Illingworth, G. D., & Franx, M. 2006, *ApJL*, 648, L5
- Overzier, R. A., Guo, Q., Kauffmann, G., et al. 2009a, *MNRAS*, 394, 577
- Overzier, R. A., Shu, X., Zheng, W., et al. 2009b, *ApJ*, 704, 548
- Papovich, C., Finkelstein, S. L., Ferguson, H. C., Lotz, J. M., & Gialalisco, M. 2011, *MNRAS*, 412, 1123
- Pforr, J., Maraston, C., & Tonini, C. 2012, *MNRAS*, 422, 3285
- Pollo, A., Guzzo, L., Le Fèvre, O., et al. 2006, *A&A*, 451, 409
- Prada, F., Klypin, A. A., Cuesta, A. J., Betancort-Rijo, J. E., & Primack, J. 2012, *MNRAS*, 423, 3018
- Press, W. H., & Schechter, P. 1974, *ApJ*, 187, 425
- Robertson, B. E., & Bullock, J. S. 2008, *ApJL*, 685, L27
- Ruiz, A. N., Padilla, N. D., Domínguez, M. J., & Cora, S. A. 2011, *MNRAS*, 1600
- Sheth, R. K., Mo, H. J., & Tormen, G. 2001, *MNRAS*, 323, 1
- Somerville, R. S., & Primack, J. R. 1999, *MNRAS*, 310, 1087
- Somerville, R. S., & Kolatt, T. S. 1999, *MNRAS*, 305, 1
- Somerville, R. S., Primack, J. R., & Faber, S. M. 2001, *MNRAS*, 320, 504
- Somerville, R. S., Hopkins, P. F., Cox, T. J., Robertson, B. E., & Hernquist, L. 2008, *MNRAS*, 391, 481
- Somerville, R. S., Gilmore, R. C., Primack, J. R., & Domínguez, A. 2012, *MNRAS*, 423, 1992
- Sousbie, T., Courtois, H., Bryan, G., & Devriendt, J. 2008, *ApJ*, 678, 569
- Spergel, D. N., Verde, L., Peiris, H. V., et al. 2003, *ApJS*, 148, 175
- Springel, V., White, S. D. M., Tormen, G., & Kauffmann, G. 2001, *MNRAS*, 328, 726
- Springel, V., White, S. D. M., Jenkins, A., et al. 2005, *Nature*, 435, 629
- Teyssier, R., Pires, S., Prunet, S., et al. 2009, *A&A*, 497, 335
- Tinsley, B. M. 1973, *ApJ*, 186, 35
- Tinsley, B. M. 1980, *FCPh*, 5, 287
- Tonini, C., Maraston, C., Devriendt, J., Thomas, D., & Silk, J. 2009, *MNRAS*, 396, L36
- Tonini, C., Maraston, C., Thomas, D., Devriendt, J., & Silk, J. 2010, *MNRAS*, 403, 1749
- de la Torre, S., Meneux, B., De Lucia, G., et al. 2011, *A&A*, 525, A125
- Vázquez, G. A., & Leitherer, C. 2005, *ApJ*, 621, 695
- White, S. D. M., & Frenk, C. S. 1991, *ApJ*, 379, 52
- Windhorst, R. A., Cohen, S. H., Hathi, N. P., et al. 2011, *ApJS*, 193, 27
- Wuyts, S., Franx, M., Cox, T. J., et al. 2009, *ApJ*, 700, 799

APPENDIX A: INTERGALACTIC MEDIUM CORRECTIONS

The MEIKSIN and INOUE-IWATA models (Meiksin 2006; Inoue & Iwata 2008) discussed in §2.5 are both based on a Monte Carlo approach that distributes LLSs chosen from a redshift distribution dN/dz and an optical depth distribution $dN/d\tau$ (both constrained by observations), and averages over the IGM transmission measured along a large number of random lines of sight. The IGM effective optical depth τ_e at observed wavelength λ is taken to be the sum of the Lyman continuum (LC) optical depth due to LLSs, the optically thin IGM, and the Ly α forest as follows:

$$\tau_e(\lambda) = \tau_{\text{LC}}^{\text{LSS}}(\lambda) + \tau_{\text{LC}}^{\text{IGM}}(\lambda) + \sum_i \bar{\tau}_i(\lambda). \quad (\text{A1})$$

The optical depth due to photoelectric absorption by LLSs along the line of sight to a source at redshift z is given by

$$\tau_{\text{LC}}^{\text{LSS}}(\lambda) = \int_{z_L}^z dz' \int_1^\infty d\tau_L \frac{\partial^2 N}{\partial \tau_L \partial z'} \left(1 - \exp \left[-\tau_L \left(\frac{1+z_L}{1+z'} \right)^3 \right] \right), \quad (\text{A2})$$

with $z_L = \lambda/912 \text{ \AA} - 1$, and $\partial^2 N / \partial \tau_L \partial z'$ the number of absorbers per unit redshift and optical depth. In the MEIKSIN model the LLSs are randomly drawn from the distributions

$$\frac{dN}{dz} = 0.25(1+z)^{1.5} \quad (\text{A3})$$

$$\frac{dN}{d\tau_L} \propto \tau_L^{-1.5}, \quad (\text{A4})$$

while INOUE-IWATA assumes

$$\frac{dN}{dz} = \frac{A}{688.4} \begin{cases} \left(\frac{1+z}{1+z_1} \right)^{\gamma_1} & (0 < z \leq z_1) \\ \left(\frac{1+z}{1+z_1} \right)^{\gamma_2} & (z_1 < z \leq z_2) \\ \left(\frac{1+z_2}{1+z_1} \right)^{\gamma_2} \left(\frac{1+z}{1+z_2} \right)^{\gamma_3} & (z > z_2) \end{cases} \quad (\text{A5})$$

$$\frac{dN}{d\tau_L} \propto \tau_L^{-1.3}, \quad (\text{A6})$$

with $A = 400$, $\gamma_1 = 0.2$, $\gamma_2 = 2.5$, $\gamma_3 = 4$, $z_1 = 1.2$, and $z_2 = 4$. The mean IGM transmission due to the LLSs typically stabilizes after averaging over $\sim 10,000$ random lines of sight. Following Meiksin (2006) and Harrison et al. (2011), both models include a static contribution from the diffuse or optically thin IGM and the Ly α forest:

$$\tau_{\text{LC}}^{\text{IGM}}(\lambda) = C(1+z_L)^{4.4} \left[\frac{1}{(1+z_L)^{3/2}} - \frac{1}{(1+z)^{3/2}} \right], \quad (\text{A7})$$

$$\bar{\tau}_n(\lambda) \equiv -\ln(\exp(-\tau_n(\lambda))), \quad (\text{A8})$$

with $C = 0.07553$ and the Lyman transitions $n \rightarrow 1$ up to $n = 31$ are included.

For completeness, we also give the MADAU modeling approximation (Madau 1995):

$$\tau_e(\lambda) = \tau_{\text{LC}}(\lambda) + \sum_{j=1,i} A_j \left(\frac{\lambda}{\lambda_j} \right)^{3.46} \quad (\text{A9})$$

$$\begin{aligned} \tau_{\text{LC}}(\lambda) &\simeq 0.25x_c^3(x_{\text{em}}^{0.46} - x_c^{0.46}) + 9.4x_c^{1.5}(x_{\text{em}}^{0.18} - x_c^{0.18}) \\ &- 0.7x_c^3(x_c^{-1.32} - x_{\text{em}}^{-1.32}) - 0.023(x_{\text{em}}^{1.68} - x_c^{1.68}), \end{aligned} \quad (\text{A10})$$

with $A_j = (0.0036, 0.0017, 0.0012, 0.00093)$ for $\lambda_j = (1216, 1016, 973, 950) \text{ \AA}$, $x_c \equiv 1 + z_c$, $x_{\text{em}} \equiv 1 + z_{\text{em}}$, $z_c =$

$\lambda/\lambda_L - 1$, and z_{em} is the redshift of the source. Eq. A10 is the approximation given for Eq. 16 in Madau (1995, see footnote 3 in that paper).

This paper has been typeset from a $\text{\TeX}/\text{\LaTeX}$ file prepared by the author.